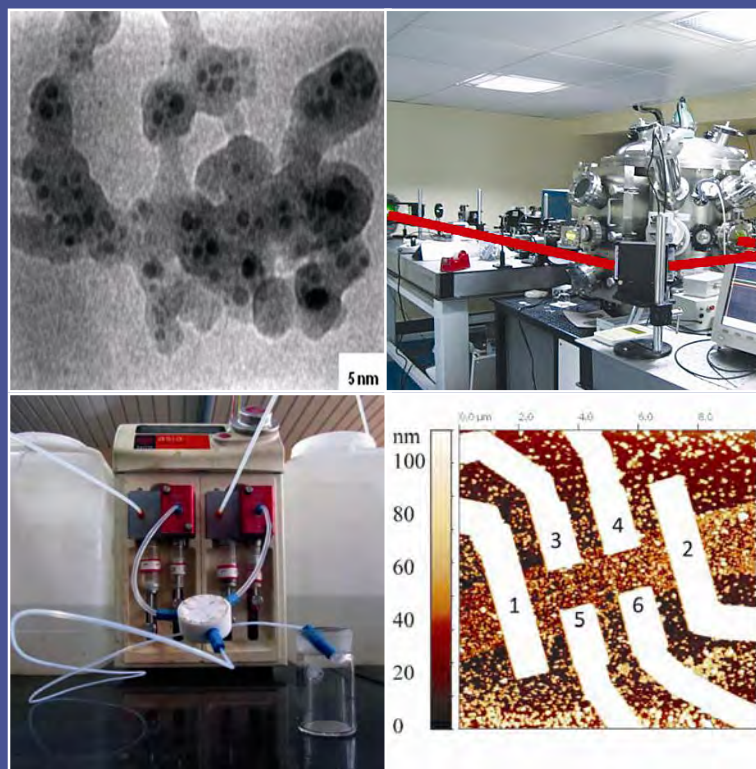


BARC

NEWSLETTER



भाभा परमाणु अनुसंधान केंद्र
BHABHA ATOMIC RESEARCH CENTRE



IN THIS ISSUE

- Designer Prussian Blue Analogues Molecular Magnets with Possible Applications
- Extraction of Uranium from Dilute Solutions using Microbore Tubes
- Development of 30 J / 300 - 800 ps (100 GW) Nd: Glass laser system for High Energy Density Physics (HEDP) Studies
- Diagnostic & Prognostic System for Identification of Accident Scenarios and Prediction of "Source Term" in Nuclear Power Plants under Accident Conditions
- Design and development of an integrated Environmental Radiation Monitor - Automatic Weather Station (ERM-AWS)
- Radiography of 140 mm Thick Weld- Multiple Film Technique

In the Forthcoming Issue

1. Indigenous Development of Carbon Aerogel Farad Super-capacitors and Application in Electronics circuits
N.C. Pramanik and Shantanu Das
2. Measurement of Mechanical Properties of a PHWR pressure tube using the in-house Developed '*In-situ* Property Measurement System (IProMS)'
S. Chatterjee et al
3. Development and Adoption of Low Sodium Glass Frit for Vitrification of High Level Radioactive Liquid Waste at Tarapur
T.P. Valsala
4. Preparation and Validation of Gas sealed High Isotopic Purity Heavy Water Reference Standards
K. Dhole et. al

CONTENTS

<i>Editorial Note</i>	ii
Brief Communications	
• Synchrotron Based Time Resolved and Energy Scanning Extended X-ray Absorption Fine Structure (EXAFS) Facilities at Indus-2: Probing Kinetics and Local Structure in Atomic Length	iii
• A Rapid, Continuous and Renewable Method for Production of The Anticancer Drug Camptothecin	iv
Research Articles	
• Designer Prussian Blue Analogues Molecular Magnets with Possible Applications <i>Pramod Bhatt, Amit Kumar and S.M. Yusuf</i>	1
• Extraction of Uranium from Dilute Solutions using Microbore Tubes <i>M. Darekar, K.K. Singh, S.S. Govalkar, J.M. Joshi, S. Mukhopadhyay, K.T. Shenoy and S.K. Ghosh</i>	9
Technology Development Articles	
• Development of 30 J / 300 - 800 ps (100 GW) Nd: Glass laser system for High Energy Density Physics (HEDP) Studies <i>S. Chaurasia, C.G. Murali, D.S. Munda, P. Leshma and R. Sabale</i>	15
• Diagnostic & Prognostic System for Identification of Accident Scenarios and Prediction of "Source Term" in Nuclear Power Plants under Accident Conditions <i>Santhosh, B. Gera, Mithilesh Kumar, I. Thangamani, M. Hari Prasad, A. Srivastava, Anu Dutta, Pavan K. Sharma, P. Majumdar, V. Verma, Sunil Ganju, V. Gopika, B. Chatterjee, R.K. Singh, K.K. Vaze and A.K. Ghosh</i>	22
• Design and development of an integrated Environmental Radiation Monitor - Automatic Weather Station (ERM-AWS) <i>A. Vinod Kumar, M.P. Ratheesh, S.S. Salunkhe, R. Jana, S.G. Gavas, T. Mukundan, P.R. Ninawe, M.S. Prakasha, S. Garg and M.D. Patel</i>	34
• Radiography of 140 mm Thick Weld- Multiple Film Technique <i>S.P. Srivastava, S.P. Pandarkar, K.B. Santhosh, G.P. Sahu and S.B. Jawale</i>	38
News and Events	
• Critical Design Review of the MACE Gamma-Ray Telescope: Status Report	45
• Report on Eleventh ISEAC International Discussion Meet on Electrochemistry and its Applications (11 th ISEAC-DM-2014)	47
• IAEA Regional Training Course on "Security in the Transport of Radioactive material"	49
• National Conference (IARPNC-2014) : a Report	51
• National Conference on Rare Earth Processing and Utilization-2014 (REPUT-2014) : a report	52
BARC Scientists Honoured	

Editorial Committee**Chairman**

Dr. S.K. Apte,
Director, Bio-Science Group

Editor

Dr. K. Bhanumurthy
Head, SIRD

Associate Editors for this issue

Dr. R.C. Hubli, MPD
Dr. S.K. Sandur, RB&HSD

Members

Dr. R.C. Hubli, MPD
Dr. D.N. Badodkar, DRHR
Dr. K.T. Shenoy, ChED
Dr. A.P. Tiwari, RCnD
Dr. S.M. Yusuf, SSPD
Dr. A.K. Tyagi, ChD
Mr. G. Venugopala Rao, APPD
Dr. C.P. Kaushik, WMD
Dr. G. Rami Reddy, RSD
Dr. S. Kannan, FCD
Dr. A.K. Nayak, RED
Dr. S.K. Sandur, RB&HSD
Dr. S.C. Deokattey, SIRD

From the Editor's Desk.....

At the outset, we would like to thank all our colleagues in BARC, who have uploaded their award winning papers for the Founder's Day Special Issue of the BARC Newsletter. I would like to inform you that we have received more than 60 papers this year.

The present issue showcases interesting R&D work carried out at BARC. First we have an article on a 30J laser system and some recent experiments on High Energy Density Physics which were done using this facility. Second, we have an article on magnetic materials (particularly Prussian blue-based molecular magnetic compounds) which are important for various technological applications.

BARC is committed to radiation protection and as a part of this commitment, BARC and ISRO under a collaborative programme have designed and integrated the Environmental Radiation Monitor (ERM, developed under IERMON program by BARC) with Automatic Weather Station (AWS, developed by ISRO), as a single stand-alone ERM-AWS system. This is being used for online monitoring of atmospheric gamma radiation. A brief description of the system is given in one of the articles.

Three of our young scientists received the INSA Medal for young scientists this year. The BARC Scientists honoured column features this achievement.

We request all our colleagues to contribute Brief Communications, Research Articles, Technology Development Articles and Feature Articles for quick publication in the BARC Newsletter, so that all our colleagues will be in touch with the latest developments at BARC.

Dr. K. Bhanumurthy
On behalf of the Editorial Committee

Synchrotron Based Time Resolved and Energy Scanning Extended X-ray Absorption Fine Structure (EXAFS) Facilities at Indus-2: Probing Kinetics and Local Structure in Atomic Length

(Physics Group)

Synchrotron based Time Resolved Extended X-ray Absorption Fine Structure (EXAFS) technique in probing *in-situ* growth of gold nanoparticles

The growth of block copolymer stabilized gold nanoparticles has been investigated by the *in-situ* time resolved synchrotron EXAFS measurement facility recently established at the Energy Dispersive EXAFS beamline (BL-08), INDUS-2 SRS. Gold nanoparticles have been synthesized by mixing aqueous solution of Chloroauric acid with sodium citrate and pluronic block copolymer P85 [1]. The block copolymer acts as a reductant as well as stabilizer. Sodium Citrate has been used as an additional reducing agent to get higher yield. The EXAFS spectra have been measured for 90 minutes at an interval of 2 minutes and the radial distribution function shows the reduction of Au-Cl bond and the appearance of Au-Au bond with time which signifies the reduction of the gold precursor to gold nanoparticle. From the spectra it is evident that after 10 minutes the growth proceeds very rapidly with a marked increase in the Au-Au peak and decrease in the Au-Cl peak.

[1] Ray et al., *Langmuir* 27, 4048(2011).

Change in cation distribution in $Ni_xZn_{1-x}Fe_2O_4$ as a function of Ni concentration studied by synchrotron EXAFS technique

Spinel ferrite samples of $Ni_xZn_{1-x}Fe_2O_4$ (for $x=0.2, 0.4, 0.5, 0.6$ and 0.8) nanoparticles prepared by a novel chemical synthesis method have been characterized by X-ray Absorption Spectroscopy (XAS) technique at the Energy Scanning EXAFS beamline (BL-09), INDUS-2 SRS. Fe edge XANES data clearly shows that as Ni concentration increases, the pre-edge feature, which is a signature of 1s to 3d quadrupole transition (allowed only in the tetrahedral symmetry), is enhanced. $ZnFe_2O_4$ is a well known normal spinel ferrite with all Zn^{2+} ions at tetrahedral sites and all Fe^{3+} ions at octahedral sites. However, $NiFe_2O_4$ has an inverse spinel structure with Ni^{2+} ions are at octahedral sites and Fe^{3+} ions are equally distributed at octahedral and tetrahedral sites. In case of $Ni_xZn_{1-x}Fe_2O_4$ sample, as more and more Ni goes to octahedral site, occupancy of Fe in tetrahedral sites is increased. A quantitative determination of the relative occupancy of iron cation in the octahedral and tetrahedral sites of the above spinel structure was obtained from EXAFS data analysis.

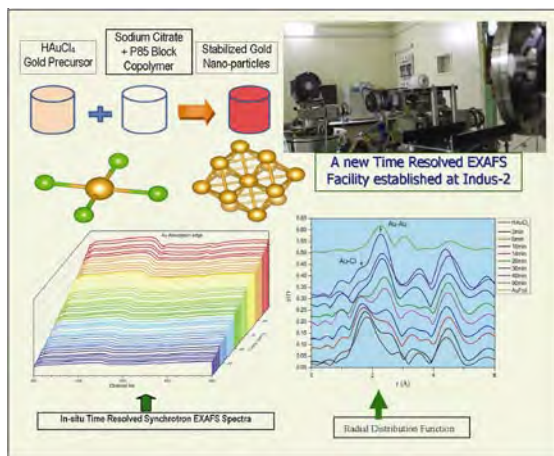
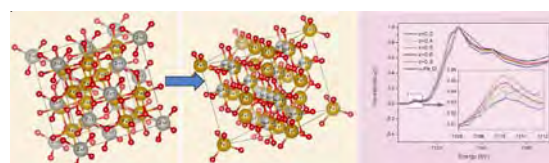


Table: Percentage of cations in octahedral and tetrahedral sites

Sample	Octahedral	Tetrahedral
$Ni_{0.2}Zn_{0.8}Fe_2O_4$	87%	13%
$Ni_{0.4}Zn_{0.6}Fe_2O_4$	79%	21%
$Ni_{0.5}Zn_{0.5}Fe_2O_4$	73%	27%
$Ni_{0.6}Zn_{0.4}Fe_2O_4$	69%	31%
$Ni_{0.8}Zn_{0.2}Fe_2O_4$	61%	39%



A Rapid, Continuous and Renewable Method for Production of The Anticancer Drug Camptothecin

(Bio-Science Group)

A promising viable technology for production of the anticancer drug camptothecin was developed using plant tissue cultures of the indigenous medicinal plant *Ophiorrhiza*. This plant is prone to seasonal and geographical variations. Camptothecin is a high value drug used in cancer therapy and effective against colon cancer. Production of camptothecin from the nature involves destruction of the various plant parts. Due to the considerable importance of camptothecin, more and more trees are uprooted which in turn results in the extinction of the species from the natural flora. A biotechnological method, using plant tissue cultures of *Ophiorrhiza* (Fig.1) for camptothecin production developed in NA&BTD, produced significant levels of camptothecin (multifold 20-25 fold) (Fig.2) during a short period of 35 days and without the destruction of the plants while plants growing in nature contained only low levels- 0.002% dry weight of the alkaloid (Roja et al., 2014). In short, the method, consists of growing the plant tissues in the laboratory, in a nutrient medium supplemented with plant growth regulators under sterile and controlled conditions of temperature and incubating them under fluorescent light. The cultures remain unaffected by external seasonal conditions and may thus be used continuously for the production of camptothecin. Tissue cultures are maintained in the laboratory by regular subculture

and therefore form a renewable source for the production of camptothecin. Additionally, the method also facilitates micropropagation of *Ophiorrhiza* plants through shoot cultures (Fig.3) (Roja 2008), which may be advantageous to preserve and conserve these endangered plants. Higher yields of camptothecin obtained in these multiple shoot cultures is a significant observation and is noteworthy since it is a prerequisite and beneficial for commercialization of any technology. Thus it provides a rapid, continuous and a renewable method for the production of camptothecin. This technology developed by Nuclear Agriculture and Biotechnology Division, Bio-Science Group of BARC was transferred to Patanjali Bio-Research Institute (PBRI), Haridwar in February 2014.

Publications:

Roja Gopalakrishnan and Bhavani Shankar (2014). Multiple shoot cultures of *Ophiorrhiza rugosa* var. decumbens Deb&Mondal -A viable renewable source for the continuous production of bioactive *Camptotheca* alkaloids apart from stems of the parent plant of *Nothapodytes foetida* (Wight.) Sleumer. *Phytomedicine* 21, 383-389.

Roja Gopalakrishnan (2008). Micropropagation and production of Camptothecin from in vitro plants of *Ophiorrhiza rugosa* var. decumbens. [Nat. Prod. Res.](#);22(12):1017-23.



Fig.1: Multiple shoot cultures of *Ophiorrhiza* species

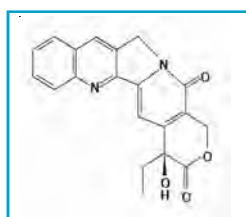


Fig.2: Camptothecin (Anticancer drug)



Fig.3: Micropropagation of the medicinal plant *Ophiorrhiza* through shoot cultures

Designer Prussian Blue Analogues Molecular Magnets with Possible Applications

Pramod Bhatt, Amit Kumar and S.M. Yusuf
Solid State Physics Division

We have investigated structural and magnetic properties of a large variety of Prussian blue based molecular magnetic compounds. These materials show promising multifunctional properties that are important for various technological applications. The present article gives an overview of some of these results.

Magnetic materials are the key components of many electronics devices for storage and retrieval of information, such as computer hard drives and video tapes. Magnetic materials are also in high demand in power generation, non-polluting electric vehicles, medical science, telecommunication, etc. Due to wide technological applications of magnetic materials, there have always been quests for new magnetic materials. Presently, an intense level of research is dedicated to fabricate new magnetic material based electronic devices. Historically, magnetic materials used so far for devices are inorganic in nature. However, organic or molecule-based materials offer possibility of using light-weight flexible materials that include magnetic functionalities. Magnets fabricated using organic/molecular compounds having unpaired electrons, located either in *s*- or *p*-orbitals (in pure organic radicals), or in *d*- or *f*-orbitals (in transition or lanthanide metal ions) are termed as molecular magnets. The first molecular ferromagnet was discovered in 1986 which was magnetically ordered at very low temperature of 4.8 K, demonstrated that a magnet could be made using organic chemistry and without usual high temperature energy intensive processing [1, 2]. This discovery opened a new branch of magnetism called molecular magnetism, with endless possibilities of tailoring new magnetic materials for organic electronics and spintronic applications by using organic, organo-metallic and coordination metal chemistry [3, 4].

The pioneering concept of “designer magnets” refers to the possibility of creating the desired magnetic materials using flexible chemical synthesis methods. Molecular magnets offer the possibility to create the magnetic system of one’s choice by changing the molecular building blocks and their arrangement in these compounds. For example, one can vary the transition metal ions to obtain various spin values. By proper choice of the organic ligands, one can tune the magnetic interaction, its symmetry, and range. Depending upon the starting organic/molecular species used for synthesis, molecule-based magnets can be purely organic or hybrid organic-inorganic. The hybrid organic-inorganic magnets are 3D compounds where the organic building blocks/ligands act as either active spin centre *i.e.* net spin localized both on metallic ions as well as on the organic species {e.g., tetracyanoethylene (TCNE)}, or passive spin centre *i.e.* net spin located mainly on the metallic site, such as hexacyanometallate or Prussian blue analogues (PBAs) based magnets. We have investigated various molecular magnetic compounds [5-36] mainly belonging to the PBA [8-36] type compounds.

Crystal structure:

The compounds of PBAs are represented by a common formula, $X_n A_k [B(CN)_6]_l \cdot mH_2O$ in which *A* and *B* are 3*d* transition metal ions which are periodically arranged in a cubic structure, and *X* is an alkali metal ion, such as K^+ or Rb^+ . The PBA compounds crystallize in a face centered cubic (*fcc*)

structure, space group $Fm\bar{3}m$, as shown in Fig. 1. The transition metal A and B ions are located at the $4a$ $(0, 0, 0)$ and $4b(1/2, 1/2, 1/2)$ crystallographic positions, respectively. The alkali metal ions and water molecules occupy the interstitial sites. Two types of water molecules *i.e.* coordinated and non-coordinated are generally present in PBA compounds depending on their stoichiometry (ratio k/l). When $k/l=1$, no $[B(CN)_6]$ vacancies are present in the structure, and only non-coordinated water molecules occupy the interstitial positions of $8c$ and $32f$. However, when $k/l > 1$, $B(CN)_6$ vacancies are present, and the crystal structure allows both types of water molecules. Besides the non-coordinated water molecules at $8c$ and $32f$ sites, the coordinated water molecules occupy the empty nitrogen sites of $[B(CN)_6]$.

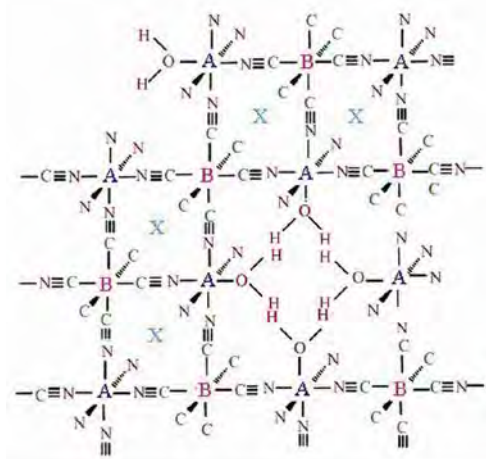


Fig. 1: Crystal structure of PBAs with general formula of $X_k A_l [B(CN)_6]_m \cdot n H_2O$. Water molecules occupy both interstitial as well as coordinated sites when $k/l > 1$. The alkali metal ions (X) also reside at interstitial positions in the structure.

Effect of crystal field on magnetic ordering

A and B ions are surrounded octahedrally by N and C, respectively, in fcc lattice (Fig. 2). Since, the N octahedra are bigger than the C octahedra, the metal ion B , surrounded by carbon octahedron, experiences a strong ligand field, resulting in a large splitting of the t_{2g} and e_g electronic levels of $3d$ orbitals. In case of B ions, the splitting energy is greater than the

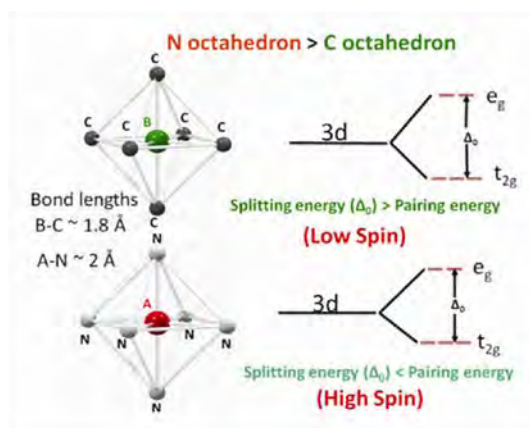


Fig. 2: Schematic representation of the C and N octahedra around the metal ions, and formation of high-spin and low-spin states in the PBAs

pairing energy, giving a low-spin state for B ions. For A ions, because of a relatively weaker ligand field of the N octahedron, usually a high spin state is observed.

The Fe^{3+} based PBA compound, $Fe[Fe(CN)_6]_2 \cdot 4H_2O$ [8,9], studied by us, shows an excellent example of high-spin and low-spin states (Fig. 3). This compound orders ferromagnetically below 17.4 K. Our low temperature neutron diffraction study revealed a ferromagnetic ordering between high spin ($S = 5/2$) and low spin ($S = 1/2$) Fe^{3+} ionic moments in this compound.

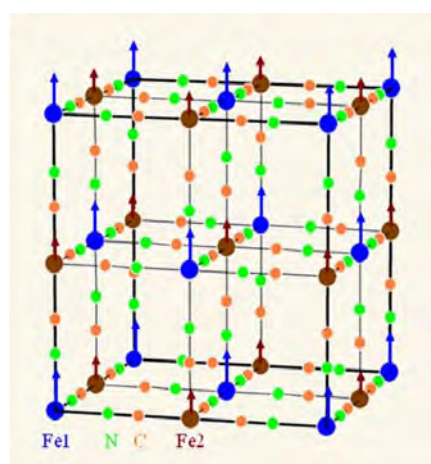


Fig. 3: Ferromagnetic ordering between high-spin ($Fe1$, $S = 5/2$) and low-spin ($Fe2$, $S = 1/2$) Fe^{3+} ions below 17.4 K in $Fe[Fe(CN)_6]_2 \cdot 4H_2O$ compound

Because of their multifunctional magnetic properties, such as photo/pressure/humidity induced magnetization, magnetic pole inversion, zero/negative thermal expansion, as well as ion sensing, and gas storage properties, these materials can be used in hydrogen gas storage, memory storage, photo switching based electronic devices, etc. [37-40] (Fig. 4).



Fig. 4: Possible multidimensional applications of Prussian blue analogues

Enhancement of magnetic ordering temperature:

Magnetic transition temperature for most of this class of compounds is well below the room temperature. Therefore, appropriate choices of the transition metal ions (*A* and *B*) and their valence modulation can enhance magnetic properties, such as magnetic exchange interaction, ordering temperature (T_c), saturation magnetization, coercive field, and remanence. We have shown that the magnetic transition temperature of thin films of PBAs $K_jFe_l[Cr(CN)_6]_2 \cdot nH_2O$ can be enhanced by varying electrode reduction voltage and deposition time in the electro-deposition method [19]. Fig. 5 shows *M* vs *T* curves at different values of thickness (a), and reduction voltage (b) for the films. As the film thickness increases from 0.5 μm to 5 μm , the T_c increases from 11 to 21 K, However, with varying reduction voltage from -0.5 to -0.9 V, the T_c increases up to ~ 65 K. The enhancement in T_c is mainly attributed to the change in the Fe(II)/Cr(III) ratio because of incorporation of K^+ ions

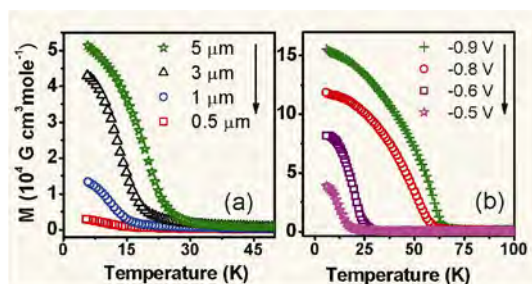


Fig. 5: The magnetization vs *T* curves at varying film thickness (a) and reduction voltage in the electro-deposition (b) for $K_jFe_l[Cr(CN)_6]_2 \cdot nH_2O$ [19].

with increasing electrode voltage. The films also show a change in color with varying reduction voltage, useful for photochromic applications.

In another example, the T_c has been enhanced by using 4*d* ion (Ru^{3+}) substitution in the cyanide-bridged molecular magnets, $Ru_xNi_{3-3x/2}[Cr(CN)_6]_2 \cdot zH_2O$ ($0 \leq x \leq 0.5$) [17] as shown in Fig. 6. The T_c increases with increasing Ru substitution. The maximum T_c of ~ 62 K has been observed for the compound with $x=0.2$. The observed variation in the T_c with composition has been understood by considering the change in effective number of the magnetic nearest neighbors and their average spin values [17].

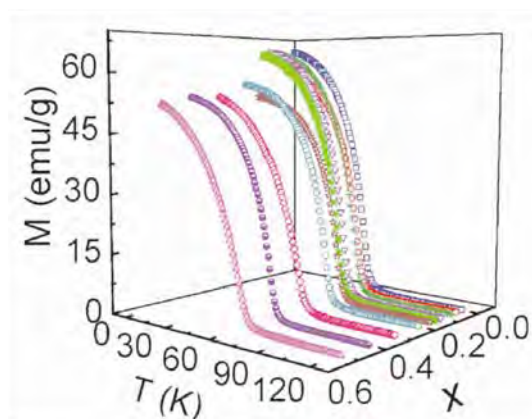


Fig. 6: The magnetization vs *T* curves as a function of Ru substitution (i.e. *x*) showing T_c variation in Ru-ni based PBA [14].

Quantification of structural disorder by reverse Monte Carlo simulation:

PBAs contain lots of vacancies as described earlier. The stoichiometry decides the $B(CN)_6$ vacancies and

the water content. We have used reverse Monte Carlo (RMC) simulation method on the neutron diffraction data to correlate magnetic properties of PBAs with their structural disorder [11,12,15,17,20,33]. The observed and the RMC fitted neutron diffraction patterns for $\text{Fe}_{1.5}[\text{Cr}(\text{CN})_6]\cdot z\text{H}_2\text{O}$ [33] are plotted in terms of the $F(Q)$, the sum of the scattering amplitudes from all the atoms in the reciprocal space at a given Q value in Fig. 7 (left). It is interesting to note that the first Bragg peak (100) is forbidden under $Fm\bar{3}m$ space group. Also, modulations in the background of the diffraction data show a large amount of diffuse scattering present in the compound. Here, we note that the forbidden Bragg peak (100) in the neutron diffraction pattern has been fitted well by RMC analysis; suggesting that this peak is related to an inherent structural disorder present in the compound.

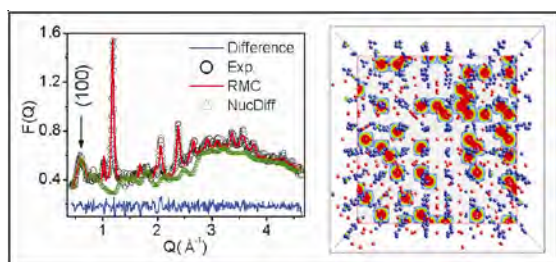


Fig. 7: (Left) The room temperature neutron diffraction pattern and the corresponding RMC simulated curve recorded for $\text{Fe}_{1.5}[\text{Cr}(\text{CN})_6]\cdot z\text{H}_2\text{O}$. (Right) Contour plot which shows the distribution and clustering of oxygen atoms after the RMC analysis[33]

The distribution of oxygen atoms in the two dimensional plots has been shown in the right panel of Fig. 7. The clustering (size $\sim 3\text{--}4 \text{ \AA}$) of the non-coordinated oxygen atoms around the coordinated oxygen atoms in the compound has been observed. Our RMC analysis shows that the oxygen clustering is mainly responsible for the structural disorder and reduction of T_c .

Particle size dependent magnetic properties:

The variation of magnetic properties with crystallite size is an important issue in the design of molecular nanomagnets for practical applications in nano-devices. We have studied the particle size

dependence of magnetic properties of nanoparticles of the $\text{Fe}[\text{Fe}(\text{CN})_6]_z\cdot\text{H}_2\text{O}$ and $\text{Cu}_{1.5}[\text{Cr}(\text{CN})_6]\cdot z\text{H}_2\text{O}$ PBA compounds using x-ray and neutron diffraction, transmission electron microscopy, and dc magnetization techniques [13,18]. The transmission electron microscopy images of nanoparticles of the $\text{Cu}_{1.5}[\text{Cr}(\text{CN})_6]\cdot z\text{H}_2\text{O}$ compound are shown in Fig. 8 (a), and the variation of saturation magnetization is shown in Fig. 8 (b). Magnetic study of the nanoparticles of above compounds has revealed weaker magnetic properties (e.g., T_c , M_{sat}) with reduced particle size due to increased surface spin disorder.

Tuning magnetism by external field:

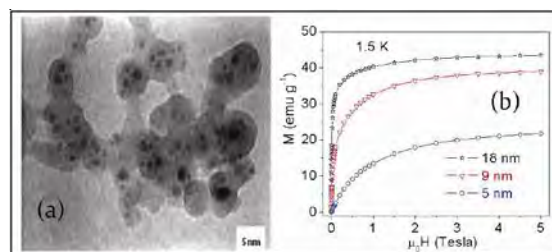


Fig. 8: (a) Transmission electron microscopy image for 5 nm, and (b) variation of magnetization with magnetic field for three different particle sizes of $\text{Cu}_{1.5}[\text{Cr}(\text{CN})_6]\cdot z\text{H}_2\text{O}$ nanoparticle [18]

We have shown an external magnetic field driven transition from an antiferromagnetic (AFM) ground state to a ferrimagnetic (FIM) state in $\text{Rb}_{0.19}\text{Ba}_{0.3}\text{Mn}_{1.1}[\text{Fe}(\text{CN})_6]\cdot 0.48\text{H}_2\text{O}$ Prussian blue analogue [28]. In the presence of an external dc magnetic field, a decrease in AFM ordering temperature and an appearance of a FIM phase is evident in ac susceptibility measurements. With increasing H , the AFM phase shrinks and the FIM phase grows, and for $H > 4\text{T}$, the AFM phase disappears completely and the system transforms to the FIM phase. An H - T phase diagram for the system is shown in Fig. 9.

Magnetization reversal and mean field calculation

We have observed a peculiar phenomenon of magnetization reversal or negative magnetization (Top layer in Fig.10) for the $\text{Cu}_{0.73}\text{Mn}_{0.77}$

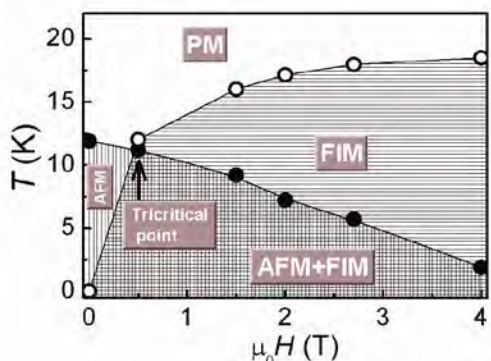


Fig. 9: Magnetic phase diagram for the $Rb_{0.19}Ba_{0.3}Mn_{1.1}[Fe(CN)_6] \cdot 0.48H_2O$ PBA system in the temperature-magnetic field plane [28]

$[Fe(CN)_6] \cdot zH_2O$ PBA system. The observed magnetization reversal has been successfully explained experimentally [15] and theoretically [16]. The molecular field theory (MFT) has been used to calculate Cu, Mn and Fe sublattice magnetizations. Under MFT, the net magnetic fields acting at the Cu, Fe and Mn sites are given by $H_{Cu} = H + \gamma_{CuFe} M_{Fe}$, $H_{Mn} = H + \gamma_{MnFe} M_{Fe}$ and $H_{Fe} = H + \gamma_{CuFe} M_{Cu} + \gamma_{MnFe} M_{Mn}$. Here, M is sublattice magnetization, H is external field, and γ_{ij} is molecular field coefficient between i^{th} and j^{th} magnetic sublattices. The γ_{ij} are related to the magnetic exchange coefficients (J_{ij}) by the relation $\gamma_{ij} = \frac{2Z_{ij}J_{ij}}{y_i N (g\mu_B)^2}$ where Z_{ij} are number of j -type magnetic neighbors surrounding an i -type ion, y_i is the molar fraction of the i^{th} ionic site, and N is the total number of magnetic ions per unit volume. The g is Lande g -factor, and μ_B is Bohr magneton. The sub-lattice magnetizations for Cu, Mn and Fe ionic-sites have the Brillouin function $B_5(x)$ dependence as given below

$$M_i = y_i \cdot N \cdot g \cdot \mu_B \cdot S_i \cdot B_{5_i} \left(\frac{g \cdot \mu_B \cdot S_i \cdot H_i}{k_B \cdot T} \right)$$

The above equations have been solved numerically to get the temperature and magnetic field dependencies of Cu, Mn and Fe sublattice magnetizations. The MFT calculated magnetization curves (Bottom layer in Fig.10) have successfully reproduced the observed magnetization reversal in this PBA system.

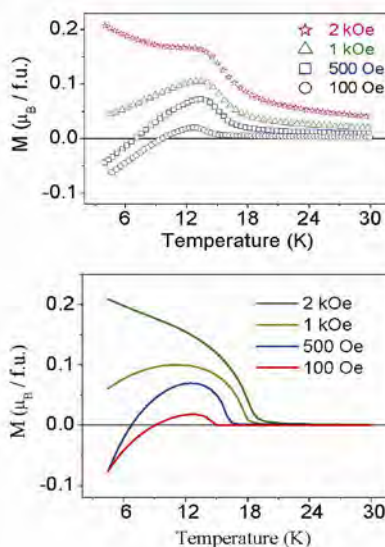


Fig.10: Observed (upper) and the MFT-calculated (lower) magnetization reversal in $Cu_{0.73}Mn_{0.77}[Fe(CN)_6] \cdot zH_2O$ PBA system [16]

Applications of PBA compounds

(a) Hydrogen storage

A possible application of PBAs is in the field of hydrogen storage [41, 42]. The presence of vacancies and interstitial sites in the crystal structure of PBAs offers an ideal platform for storage of hydrogen in such compounds. We have recently synthesized $Mn_{1.5}[Cr(CN)_6] \cdot mH_2O @ Ni_{1.5}[Cr(CN)_6] \cdot nH_2O$ core-shell structure of PBAs in order to improve the hydrogen storage capacity [42]. We have observed that the core-shell compound shows an

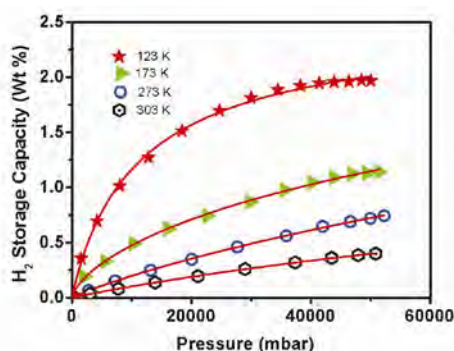


Fig. 11: The hydrogen adsorption isotherms of the $Mn_{1.5}[Cr(CN)_6] \cdot mH_2O @ Ni_{1.5}[Cr(CN)_6] \cdot nH_2O$ core-shell PBA compound at various temperatures [42]

enhancement in the hydrogen capacity (of ~ 2.0 wt % at 123 K, shown in Fig. 11) as compared to other previously reported PBAs molecular magnets [42].

(b) Magnetic random access memory

In another example, where $\text{Cu}_{0.73}\text{Mn}_{0.77}[\text{Fe}(\text{CN})_6]\cdot z\text{H}_2\text{O}$ PBA compound shows the magnetization reversal phenomenon, the possible application of this phenomenon as a bipolar switching of magnetization (using low magnetic fields) has been demonstrated [16]. Fig. 12 shows the flipping of the field-cooled magnetization of the PBA in real time under two different values of external magnetic field [16]. The magnetic-field-controlled bistable switching of the magnetization has the potential for its usage in magnetic memory applications.

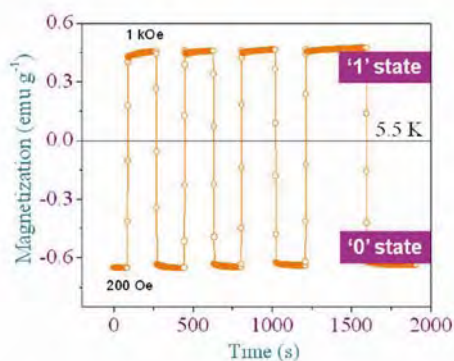


Fig.12: The magnetization switching between positive and negative values for $\text{Cu}_{0.73}\text{Mn}_{0.77}[\text{Fe}(\text{CN})_6]\cdot z\text{H}_2\text{O}$ at 5.5 K by varying the magnetic field in the sequence: 200 Oe — 1000 Oe — 200 Oe — from left [16].

(c) Applications exploiting magnetic entropy

The sign reversal of magnetic entropy change ($-\Delta S_m$) under varying temperature in systems showing a magnetization sign reversal can have practical applications. For example, the studied molecular PBA compound $\text{Cu}_{0.73}\text{Mn}_{0.77}[\text{Fe}(\text{CN})_6]\cdot z\text{H}_2\text{O}$ (which depicts magnetization reversal) also shows both positive and negative magneto-caloric effects (MCEs) below its magnetic ordering

temperature as depicted in Figure 13. The observed bipolar MCE in the $\text{Cu}_{0.73}\text{Mn}_{0.77}[\text{Fe}(\text{CN})_6]\cdot z\text{H}_2\text{O}$ compound may be utilized in a constant temperature bath application [16] as explained below. The $\text{Cu}_{0.73}\text{Mn}_{0.77}[\text{Fe}(\text{CN})_6]\cdot z\text{H}_2\text{O}$ compound as a refrigerant in a magnetic refrigerator would give an equilibrium temperature of 13 K. When any temperature fluctuation that tries to raise the temperature of the magnetic refrigerator above 13 K, the normal MCE ($-\Delta S_m > 0$) in $\text{Cu}_{0.73}\text{Mn}_{0.77}[\text{Fe}(\text{CN})_6]\cdot z\text{H}_2\text{O}$ compound will bring down the temperature of the system to 13 K. On the other hand, when the temperature of magnetic refrigerator goes down below 13 K, the inverse MCE ($-\Delta S_m < 0$) will produce heating, and the temperature of the system will rise back to 13 K. In other words, any temperature fluctuation in the vicinity of 13 K would be compensated by the two opposite MCEs, and the system ($\text{Cu}_{0.73}\text{Mn}_{0.77}[\text{Fe}(\text{CN})_6]\cdot z\text{H}_2\text{O}$ compound in a magnetic refrigerator) has the potential for its use as a constant temperature bath of 13 K.

(d) Application in radioactive waste management

PB and its analogues find their applications in waste management as well. The radio-isotopes of ^{134}Cs and ^{137}Cs , with 2.06 and 30 years half-life, respectively, are hazardous as they radiate beta-particles and strong gamma rays. In this regard, the

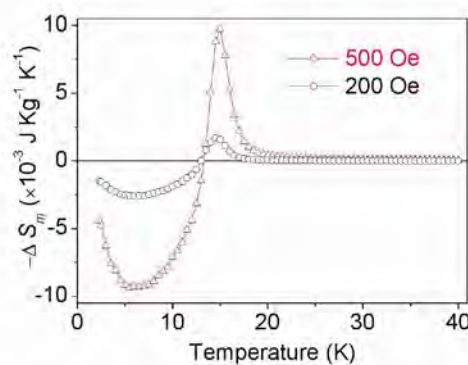


Fig. 13: The magnetic entropy change ($-\Delta S_m$) vs. T for $\text{Cu}_{0.73}\text{Mn}_{0.77}[\text{Fe}(\text{CN})_6]\cdot z\text{H}_2\text{O}$ compound at 200 (o) and 500 (Δ) Oe fields.[16]

PBAs can be used to remove radioactive $^{134}\text{-Cs}$ and $^{137}\text{-Cs}$ elements [43]. Moreover, PBAs can be used as a medicine for removing radioactive as well as nonradioactive elements (cesium and thallium) from the body. PBA traps cesium and thallium compounds in the intestines, and keeps them away from being re-absorbed by the body. The radioactive materials then move through the intestines and are passed (excreted) in bowel movements. Moreover, Prussian blue reduces the biological half-life of cesium from about 110 days to about 30 days and for thallium from about 8 days to about 3 days. Recent literature describes that magnetic Prussian blue/graphene oxide nanocomposites have been used for the removal of radioactive cesium in water [43].

(e) PB graphene devices for spintronics

Very recently, one of us fabricated micro-devices [Figure 14] comprising of graphene-PB composites for their possible device applications [36]. Graphene is considered an attractive material for spintronics applications [44], the effect of a non-covalently attached PB molecular magnet on the electronic transport properties of graphene has, therefore, been studied. Remarkably, the electronic transport properties of graphene are largely preserved after the ~ 40 nm thick PB coating. The results clearly indicate that strategies involving covalent functionalization of graphene to achieve stronger magnetic exchange coupling should be devised.

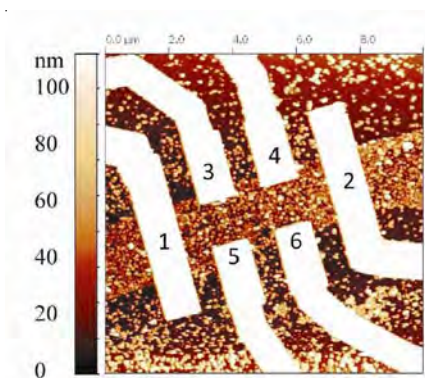


Fig. 14: PB-graphene composite micro-device for its possible application in spintronics[36].

Summary

The Prussian blue analogues molecular magnets have great potential for technological applications in information storage, displays, or as components in electronic or spintronic devices. However, commercially, it is still in the state of exploration of devices working at ambient conditions. It is uncertain to predict the timescale before any molecule-based room-temperature magnetic device may reach the market. However, with the unique properties of low weight (density: $\sim 1\text{g/cc}$), low-cost synthesis, biocompatibility, flexibility, multifunctional magnetic properties, etc., there is an immense scope of using such materials for possible technological applications in near future.

References

1. J.S. Miller, J.C. Callabrese, H. Rommelmann et al. *J. Am. Chem. Soc.* 109, 769 (1987).
2. S. Chittipedi, K.R. Cromack, J.S. Miller et al., *Phys. Rev. Lett.* 58, 2695 (1987).
3. J. S. Miller, *Adv. Mater.* 14, 1105 (2002).
4. J.M. Manriquez, G. T. Yee, R.S. McLean, A.J. Epstein, and J.S. Miller, *Science* 252, 1415 (1991).
5. P. Bhatt and S.M. Yusuf, *Surf. Sci.* 605, 1861 (2011).
6. P. Bhatt, N.Thakur, S.S. Meena, M.D. Mukadam, and S.M. Yusuf, *J. Mat. Chem. C* 1, 6637 (2013).
7. P. Bhatt, N. Thakur, M.D. Mukadam, S.S. Meena, and S.M. Yusuf, *J. Phys. Chem. C* 118, 1864 (2014).
8. A. Kumar, S.M. Yusuf, *Pramana-J. Phys.* 63,239 (2004).
9. A. Kumar, S.M. Yusuf and L. Keller, *Phys. Rev. B* 71, 054414 (2005).
10. A. Kumar and S.M. Yusuf, *Physica B* 362, 278 (2005).
11. A. Kumar, S.M. Yusuf, L Keller, *Physica B* 385–386, 444 (2006).

12. A. Kumar, S.M. Yusuf, L. Keller, J.V. Yakhmi, J. K. Srivastava, P.L. Paulose, *Phys. Rev. B* 75, 224419 (2007).
13. M.D. Mukadam, A. Kumar, S.M. Yusuf, J.V. Yakhmi, R. Tewari, G.K. Dey, *J. Appl. Phys.* 103, 123902 (2008).
14. N. Sharma, S.M. Yusuf, A. Kumar, and J.V. Yakhmi, *AIP Conf. Proc.* 1003, 8 (2008).
15. A. Kumar, S.M. Yusuf, L. Keller, and J.V. Yakhmi, *Phys. Rev. Lett.* 101, 207206 (2008).
16. S.M. Yusuf, A. Kumar, and J.V. Yakhmi, *Appl. Phys. Lett.* 95, 182506 (2009).
17. S.M. Yusuf, N. Thakur, A. Kumar, and J.V. Yakhmi, *J. Appl. Phys.* 107, 053902 (2010).
18. A. Kumar, S.M. Yusuf, and J.V. Yakhmi, *Appl. Phys. A* 99, 79 (2010).
19. P. Bhatt, S.M. Yusuf, M.D. Mukadam, and J. V. Yakhmi, *J. Appl. Phys.* 108, 023916 (2010).
20. N. Thakur, S.M. Yusuf and J.V. Yakhmi, *Phys. Chem. Chem. Phys.*, 12, 12208 (2010).
21. P. Bhatt, S.M. Yusuf, M.D. Mukadam and J.V. Yakhmi, *AIP Conf. Proc.* 1313, 186 (2010).
22. N. Thakur, S.M. Yusuf and J.V. Yakhmi, *AIP Conf. Proc.* 1347, 145 (2011).
23. N. Thakur, S.M. Yusuf, A. Kumar, and J.V. Yakhmi, *BARC Newsletter* Oct, 413 (2011).
24. V. K. Sharma, S. Mitra, A. Kumar, S.M. Yusuf, F. Juranyi, and R. Mukhopadhyay, *J. Phys.: Condens. Matter* 23, 446002 (2011).
25. R. Rao, A. Kumar and S.M. Yusuf, *AIP Conf. Proc.* 1349, 123 (2011).
26. P. Bhatt, S.M. Yusuf, M.D. Mukadam and J.V. Yakhmi, *AIP Conf. Proc.* 1347, 61 (2011).
27. V.K. Sharma, S. Mitra, A. Kumar, S.M. Yusuf, F. Juranyi, R. Mukhopadhyay, *AIP Conf. Proc.* 1447, 949 (2012).
28. S.M. Yusuf, N. Thakur, M. Medarde, and L. Keller, *J. Appl. Phys.* 112, 093903 (2012).
29. N. Thakur, S.M. Yusuf, P.L. Paulose, and L. Keller, *J. Appl. Phys.* 111, 063908 (2012).
30. P. Bhatt, S.M. Yusuf, R. Bhatt and G. Schuetz, *Appl. Phys. A* 109, 459, (2012).
31. P. Bhatt, R. Bhatt, and S.M. Yusuf, *AIP Conf. Proc.* 1447, 229 (2012).
32. A. Kumar, *BARC Newsletter*, Special issue, 190 -193, October 2013.
33. P. Bhatt, N. Thakur, M.D Mukadam, S.S. Meena, and S.M. Yusuf, *J. Phys. Chem. C* 117, 2676 (2013)
34. P. Bhatt, S.M. Yusuf, R. Bhatt, and G. Schuetz *J. Solid State Electrochem.* 17, 1285 (2013).
35. P. Bhatt, R. Bhatt, M.D. Mukadam, and S.M. Yusuf, *AIP Conf. Proc.* 1512, 1082 (2013).
36. A. Kumar, E.C. Peters, and M. Burghard, *RSC Advances* 4, 18061 (2014).
37. H. Tokoroa and S.I. Ohkoshi, *Dalton Trans.* 40, 6825 (2011).
38. S.I. Ohkoshi, Y. Abe, A. Fujishima, and K. Hashimoto, *Phys. Rev. Lett.* 82, 1285 (1999).
39. O. Sato, T. Iyoda, A. Fujishima, and K. Hashimoto, *Science* 272, 704 (1996).
40. A.L. Goodwin, K. W. Chapman, and C. J. Kepert, *J. Am. Chem. Soc.* 127, 17980 (2005).
41. S.S. Kaye, J.R. Long, *J. Am. Chem. Soc.* 127, 6506 (2005).
42. P. Bhatt, M.D. Mukadam, S. Banerjee, S. Anwar, S.S. Meena, and S.M. Yusuf, Submitted ACS applied materials and interfaces (2014).
43. H. Yang, Lei Sun, Jiali Zhai, H. Li, Yan Zhao and Hongwen Yu, *J. Mater. Chem. A*, 2, 326 (2014).
44. A.K. Geim and K.S. Novoselov, *Nat Mater* 6, 183 (2007).

Extraction of Uranium from Dilute Solutions using Microbore Tubes

M. Darekar, K.K. Singh, S.S. Govalkar, J.M. Joshi,
S. Mukhopadhyay and K.T. Shenoy
Chemical Engineering Division
and
S.K. Ghosh
Chemical Engineering Group

Abstract

Single-stage micro-scale solvent extraction of uranium from dilute solutions is studied using PTFE microbore tubes. Effects of flow rate, diameter and length of microbore tube on stage efficiency, pressure drop and settling behavior of dispersion are studied to identify the configuration that can ensure high stage efficiency (>90%) with quick settling and low pressure drop (< 2 bar). Two such configurations are put in parallel to demonstrate single-stage extraction at 1 LPH total throughput. Finally, single-stage extraction and stripping experiments with 1N NaHCO₃ as the strippant are carried out to demonstrate the possibility of concentrating uranium in the aqueous phase. Specific extraction rate in the micro-scale extractor based on microbore tubes is estimated to be more than four times of the same in a mixer-settler.

Introduction

Microchannels offer several advantages such as high surface to volume ratio, high specific interfacial area for two-phase reactions and mass transfer operations, small inventories and confident scale-up. These advantages can be harnessed for achieving process intensification. Advantages specific to solvent extraction are controllable quality of dispersion and narrow drop size distributions¹ leading to quick settling, high overall volumetric mass transfer coefficients compared to conventional extractors² and confident scale-up³. Several recent studies carried out at Chemical Engineering Division, BARC highlight potential of microchannels as process intensifying solvent extraction contactors⁴⁻⁶. In this study, microbore tubes, arguably the cheapest available microchannels are used to study extraction of uranium from dilute streams.

Experimental Work

Phase System

The aqueous phase is a simulated dilute solution having less than 1000 ppm uranium. Acidity of the

aqueous phase is 1N. The organic phase is 30% (v/v) TBP in dodecane. Distribution coefficient for extraction is about 6.7. Strippant used is 1 N NaHCO₃ due to its very low distribution coefficient.

Experimental Setup

Fig.1 shows the experimental setup used in the experiments with single microbore tubes. The setup consists of an opposed T-junction of 750 μm drilled in a PTFE disk having a microbore tube connected to it using a threaded connector. Dispersion generated at the opposed T-junction passes through the microbore tube and gets collected in a glass sample bottle which allows visual observation of settling behavior. The aqueous sample is analyzed for uranium concentration using inductively coupled plasma atomic emission spectrometer (ICP-AES, model ULTIMA-2, Make Jobin Horiba, France). The setup with two microbore tubes in parallel, used for experiments at 1 LPH total throughput, is similar to the setup shown in Fig. 1 but has two additional 2 mm diameter Y-junction distributors drilled in PTFE



Fig. 1: Experimental setup used in the experiments with single microbore tubes

disks for splitting of the aqueous and organic streams and a pipe settler (volume 15ml) for settling of dispersion.

Calculations

Equations (1)-(3) are used to quantify the experimental results. To compare the performance of different extractors SER (Specific Extraction Rate) which represents the number of moles extracted per unit time per unit volume of the extractor is used.

$$\eta = \frac{C_{AE}^{in} - C_{AE}^{out}}{C_{AE}^{in} - \frac{C_{OE}^{out}}{K_D}} \times 100 \quad (1)$$

$$PE = \frac{C_{AE}^{in} - C_{AE}^{out}}{C_{AE}^{in}} \times 100 \quad (2)$$

$$SER = \frac{(C_{AE}^{in} - C_{AE}^{out})Q_{AE}}{V} \quad (3)$$

Where, η and PE represent percentage stage efficiency and percentage extraction, respectively. C_{AE}^{in} is the concentration of uranium in the aqueous feed to the extraction stage, C_{AE}^{out} is the concentration of uranium in the raffinate from the extraction stage, C_{OE}^{out} is the concentration of uranium in the loaded organic leaving the extraction stage. K_D is distribution coefficient. Q_{AE} is the aqueous phase flow rate in the extraction stage.

V is the total volume of the extractor including the settler.

Experiments with Single Microbore Tubes

Effect of Flow Rate

Experiments were carried out to find out the maximum flow rate a single microbore tube can handle while giving quick phase separation (instantaneous phase separation with clear aqueous and organic phases and no dispersion band seen in glass sample bottle). This maximum flow rate is expected to reduce with reduction in diameter as increased velocities will make the dispersion finer, leading to difficult settling. Thus of the three available diameters (300 μm , 500 μm and 800 μm) 800 μm microbore tube was chosen for these experiments. O/A ratio was 1. Total flow rate was varied in the range 0.03-1.2 LPH. Settling was slow for flow rates more than 0.6 LPH. The flow patterns observed in 800 μm microbore tubes for the same phase system sans uranium and corresponding settling behavior are shown in Fig. 2. The dispersion becomes finer as the flow rate increases leading to difficult phase separation. For the system containing uranium, quick settling was observed up to 0.6 LPH total flow rate at O/A = 1. Fig. 3 shows the variation of stage efficiency and percentage extraction with flow rate. From 0.03 LPH to 0.6 LPH, stage efficiency reduces monotonically. In this range flow pattern is slug flow and reduction in stage efficiency is due to reduction in contact time. When flow rate is

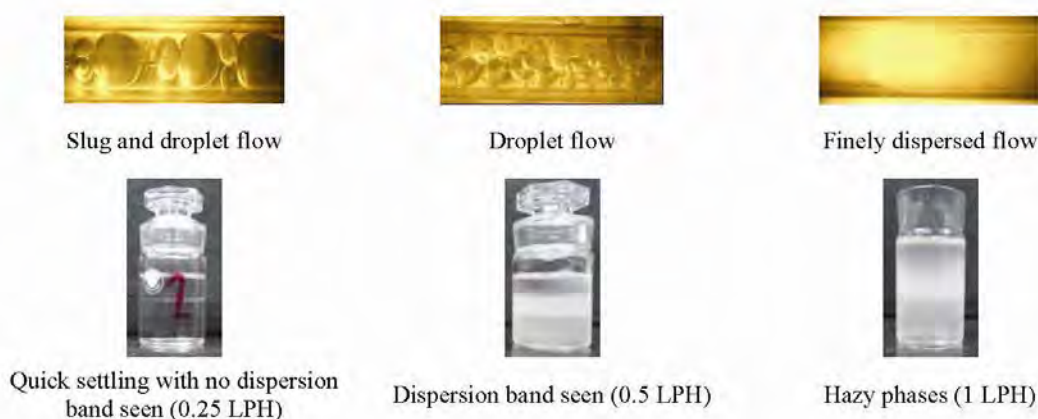


Fig. 2: Flow patterns and settling behavior of dispersion of 3N nitric acid – 30% TBP in dodecane system generated at 750 μm opposed T-junction connected to a 800 μm tube. O/A = 1/1.

increased beyond 0.6 LPH, oscillatory trends, attributable to transitions in flow pattern and combined effect of increase in specific interfacial area and reduction in contact time, are observed. Though for flow rates less than 0.6 LPH higher stage efficiencies are observed, choosing a flow rate lower than 0.6 LPH will reduce the capacity. Lower stage efficiency at 0.6 LPH can be increased by using longer tubes. Thus 0.6 LPH is taken as the maximum flow rate microbore tube of 800 μm diameter can handle.

Effect of Microbore Tube Diameter

Further experiments were done to check if 0.6 LPH flow rate can also be handled by microbore tubes of smaller diameters. Fig. 4 shows that stage efficiency increases with reduction in microbore tube diameter. Table 1 documents the pressure drop and settling behavior observed for microbore tubes of different diameters and shows that 300 μm microbore tube cannot be used despite giving the

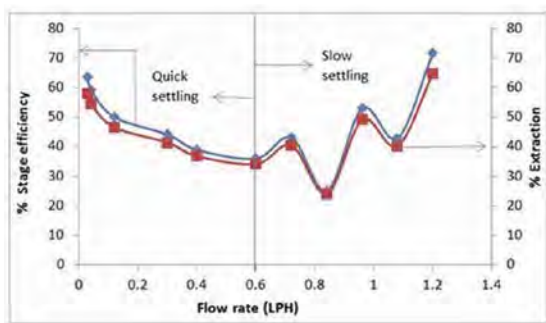


Fig. 3: Effect of flow rate on stage efficiency and percentage extraction. d = 800 μm, L = 17 cm, O/A=1/1.

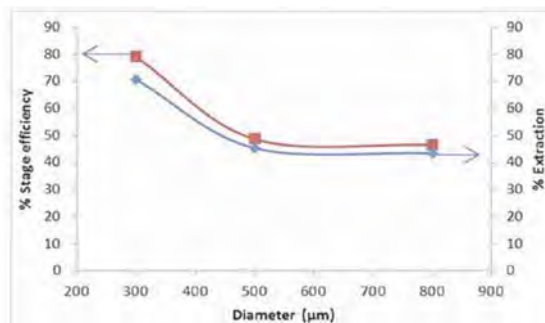


Fig. 4: Effect of microbore tube diameter on stage efficiency and percentage extraction. Q = 0.6 LPH, τ = 0.5 s, O/A = 1/1.

Table 1: Effect of microbore tube diameter on stage efficiency, pressure drop and settling

d (μm)	L (cm)	Q (LPH)	τ (s)	O/A	η	PE	ΔP (bar)	Settling
300	120	0.6	0.5	1/1	80	71	21	Very slow
500	43	0.6	0.5	1/1	49	46	4	Fast
800	18	0.6	0.5	1/1	46	43	1	Fast

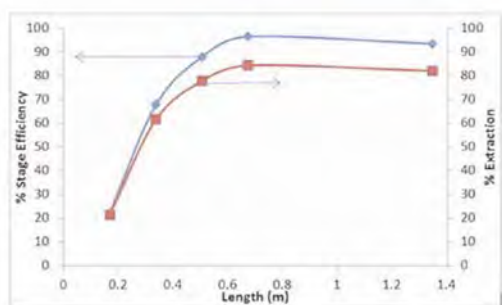


Fig. 5: Effect microbore tube length on stage efficiency. $d = 800 \mu\text{m}$, $Q = 0.6 \text{ LPH}$, $O/A = 1/1$

highest stage efficiency as pressure drop is very high and settling is very slow. For $500 \mu\text{m}$ microbore tube also pressure drop is more than 2 bar, the maximum admissible limit set by us. Thus of the three diameters $800 \mu\text{m}$ is considered as the one capable of handling high throughput with quick settling and low pressure drop. d , L , Q , τ and ΔP in Table 1 represent diameter of the microbore tube, length of the microbore tube, total flow rate, contact time and pressure drop, respectively.

Effect of Length of Microbore Tube

Further experiments were carried out to find out to what extent stage efficiency can be improved by increasing the length without breaching the upper limit on the pressure drop. Changing of contact time by changing length of microbore tube ensures that the quality of dispersion remains same and thus settling is not affected. Fig. 5 shows the effect of length of microbore tube on stage efficiency and percentage extraction. Table 2 compiles the data resulting from this set of experiments. Stage

efficiency increases with increase in the length of microbore tube when it is increased from 16 cm to 67 cm, thereafter the increase is not significant. Pressure drop is not more than 2 bar despite increase in length. Thus the optimum configuration, highlighted in bold font in Table 2, giving high stage efficiency, quick settling and low pressure drop consists of a 67 long microbore tube of diameter $800 \mu\text{m}$ connected to an opposed T-junction of $750 \mu\text{m}$ diameter. The maximum capacity of the configuration is 0.6 LPH and stage efficiency obtained at $O/A = 1/1$ is 95% in contact time of 2 sec.

Experiments with Parallel Microbore Tubes

Experiments at Total Throughput of 1 LPH

To achieve higher throughputs multiple optimum configuration can be arranged in parallel. Number of parallel paths can be decided considering that flow through each path should not exceed 0.6 LPH. For 1 LPH total throughput, experiments were conducted using two parallel paths. Table 3 summarizes the results and shows that high stage efficiency (90-100%) can be achieved with short contact time of 2.5 sec for O/A ratio ranging from $1/2$ to $2/1$ at total throughput of 1 LPH.

Comparison of Micro-scale Extractor with a Mixer-settler

Table 4 shows comparison of the micro-scale extractor and a mixer-settler. V_m and V_s represent mixer and settler volumes, respectively. For the micro-scale extractor data given in the second row of Table 3 are used. Contact time in the micro-scale extractor is very small (2.5 sec) causing inventory of

Table 2: Effect of microbore tube length on stage efficiency, pressure drop and settling

d (μm)	L (cm)	Q (LPH)	τ (s)	O/A	η	PE	ΔP (bar)	Settling
800	16	0.6	0.5	1/1	22	21	1	Fast
800	34	0.6	1.0	1/1	68	60	1	Fast
800	50	0.6	1.5	1/1	88	78	1	Fast
800	67	0.6	2.0	1/1	95	84	1	Fast
800	135	0.6	4.0	1/1	95	84	2	Fast

Table 3: Results of experiments carried out at 1 LPH total throughput

d (μm)	L (cm)	Q (LPH)	τ (s)	O/A	η	PE	ΔP (bar)	Settling
800	67	1.0	2.5	1/2	100	67	1	Fast
800	67	1.0	2.5	1/1	96	87	1	Fast
800	67	1.0	2.5	2/1	93	97	1	Fast

Table 4: Comparison of the micro-scale extractor with a mixer-settler

	Micro-scale extractor		Mixer-settler	
	Basis	Value	Basis	Value
Q (LPH)	Experiment	1	Same as in the micro-scale extractor	1
τ (sec)	Experiment	2.5	Typical value	60.0
V _m (ml)	V _m = τ Q	0.69	V _m = τ Q	16.67
V _s (ml)	Experiment	15.00	V _s = 3 V _m	50.00
SER (mol sec ⁻¹ m ⁻³)	0.027		0.006	

liquid in it to be very small compared to a mixer-settler. Values used to estimate SER for a mixer-settler (τ = 60 sec, V_s = 3V_m) are typical values used for mixer-settler. As shown in Table 4, SER in the micro-scale extractor is estimated to be more than four times of the same in a mixer-settler.

Extraction and Stripping Experiments

In these experiments uranium from a dilute aqueous stream is first extracted using 30% TBP in dodecane in a single-stage contact in the micro-scale extractor. The loaded organic is then stripped using 1N NaHCO₃ in a single-stage contact in the micro-scale extractor. The results obtained from these experiments are summarized in Table 5. C_{AS}^{out} represents the

concentration of uranium in the aqueous product stream from the stripping stage. With O/A = 1 in extraction and O/A = 2 in stripping the concentration of uranium in the raffinate and the product was 68 and 1260 ppm, respectively. With O/A = 2 in extraction and O/A = 4 in stripping, the concentration of uranium in raffinate and the product was 30 and 1159 ppm respectively. These concentrations of uranium in the aqueous product stream from the stripping stage may not be enough for direct precipitation. For higher uranium concentration in the aqueous product stream obtained from the stripping stage, a two-step procedure can be adopted. In the first step uranium can be concentrated in the organic phase by keeping

Table 5: Results of extraction and stripping experiments (feed concentration = 734 ppm)

Extraction O/A	Stripping O/A	C _{AE} ^{out} (ppm)	C _{AS} ^{out} (ppm)
1	2	68	1260
2	4	30	1159
1/2	4	173	3620

low O/A in the extraction stage. In the second step uranium should be concentrated in the strippant by keeping high O/A ratio in stripping. For $O/A = 1/2$ in extraction stage and $O/A = 4$ in the stripping stage a high uranium concentration of 3620 ppm could be achieved in the aqueous product stream from the stripping stage. But, due to low O/A in the extraction stage, concentration of uranium in the raffinate was 173 ppm. In this study only single-stage experiments are carried out. However, it is expected that in a multistage contact with $O/A = 1/2$ in extraction and $O/A = 4$ in stripping, low concentration of uranium in raffinate as well as high concentration of uranium in the aqueous product stream from stripping can be achieved.

Conclusions

Micro-scale extraction of uranium from dilute solutions is studied using microbore tubes. A configuration consisting of a 750 μm opposed T-junction having microbore tube of diameter 800 μm and length 67 cm on its downstream side is identified as the optimum configuration that can handle a total throughput of 0.6 LPH while giving 95% stage efficiency in contact time of 2 sec with quick settling of resulting dispersion and less than 1 bar pressure drop. Micro-scale solvent extraction at total throughput of 1 LPH is demonstrated using two parallel paths of this optimum configuration. Using single-stage extraction and stripping, high concentration of uranium in the product could be obtained. Specific extraction rate in the micro-scale extractor is estimated to be more than 4 times of the same in a mixer-settler. The study highlights possibility of intensification and confident scale-up

of solvent extraction process for recovery of uranium from dilute solutions by using micro-scale extractors.

References

1. Sugiura S., Nakajima M., Tong J., Nabetani H., Seki M. "Preparation of monodispersed solid lipid microspheres using a microchannel emulsification technique". *Journal of Colloid and Interface Science*, 227 (2000) 95-103.
2. Kashid M.N., Renken A., Kiwi-Minsker L. "Gas-liquid and liquid-liquid mass transfer in microstructured reactors". *Chemical Engineering Science*, 66 (2011) 3876-3897.
3. Tonkovich A., Kuhlmann D., Rogers A., McDaniel J., Fitzgerald S., Arora R., Yuschak T. "Microchannel technology scale-up to commercial capacity". *Chemical Engineering Research and Design*, 83 (2005) 634-639.
4. Darekar M., Sen N., Singh K.K., Mukhopadhyay S., Shenoy K.T., Ghosh S.K. "Liquid-liquid extraction in microchannels with Zinc-D2EHPA system". *Hydrometallurgy*, 144-145 (2014) 54-62.
5. Darekar M., Singh K.K., Mukhopadhyay S., Shenoy K.T., Ghosh S.K. "Solvent extraction in microbore tubes with UNPS - TBP in dodecane system". *Separation and Purification Technology*, 128 (2014) 96-105.
6. Sen N., Darekar M., Singh K.K., Mukhopadhyay S., Shenoy K.T., Rao H., Ghosh S.K. "Solvent extraction and stripping studies in microchannels with TBP nitric acid system". *Solvent Extraction and Ion Exchange*, 32 (2014) 281-300.

Development of 30 J / 300 - 800 ps (100 GW) Nd: Glass laser system for High Energy Density Physics (HEDP) Studies

S. Chaurasia, C.G. Murali, D.S. Munda, P. Leshma and R. Sabale
High Pressure & Synchrotron Radiation Physics Division

High energy density physics (HEDP) studies are important for several applications such as Inertial confinement fusion (ICF), x-ray source generation, weapon Physics and fundamental Science studies. To scale up the experimental capabilities in HEDP studies, we have up-graded our existing laser system to achieve 30 J energy (focusable intensity $\sim 1 \times 10^{15} \text{ W/cm}^2$). A new vacuum chamber with 42 diagnostics ports along with fifteen plasma diagnostics has been installed for laser plasma experiments. In this letter, we will briefly discuss about the laser system and some of the recent experiments done on laser driven dynamic shock studies using this facility.

Introduction

Neodymium-doped glass (Nd: Glass) was first demonstrated as a laser medium by Snitzer in 1961. Since then, it has been studied extensively for the development of high energy short pulse lasers due to its following advantages: shorter wavelength resulting in higher absorption in metals and higher process efficiency, higher electrical efficiency in case of diode pumping, and easier access for numerous applications. Globally several high peak power solid state laser systems such as Rutherford Appleton Lab (RAL) UK, National ignition facility (NIF) USA, OSAKA lab, Japan, Laser Megajoule (LMJ) France, etc have been developed for HEDP studies and various experiments on material properties studies, opacity measurement, Astrophysics and space Physics, Hydrodynamics are being conducted worldwide¹.

In this letter we will describe our achievement in the development of high power laser system and its application in the HEDP studies. This system is capable of producing several tens of Mbar pressure in targets. We will briefly report on the Equation of state (EOS) measurement of polymer and metals, shock amplification technique and the mitigation of instabilities which is the main obstacle in the success of fusion research.

Laser development

The present laser system consists of a commercial oscillator, operating at 10Hz with output energy of 100 mJ per pulse and peak to background contrast ratio of $10^5: 1$, and six amplifier stages (A1 to A6) providing output energy of 30J. First amplifier stage is of 19 mm diameter and 300 mm of length pumped with six flash lamps while the final amplifier is 75 mm of diameter and 300 mm of length pumped by eighteen flash lamps. To improve the beam quality, two spatial filters are placed between A2 and A3 as well as between A4 and A5 stages. Two Faraday Isolators are installed in the chain to prevent any optical damage due to back scattered light from various stages and from target. The schematic and photograph of the 30 J laser system is shown in the Figs.1a & 1b.

Characterization studies of 75 mm Nd: Glass amplifier

Characterization of 75mm amplifier (A6) was performed by studying various parameters such as the output laser beam profile, radial gain variation, single pass gain and thermally induced depolarization. The laser beam profile at the output of A6 was recorded using photo-paper. The beam

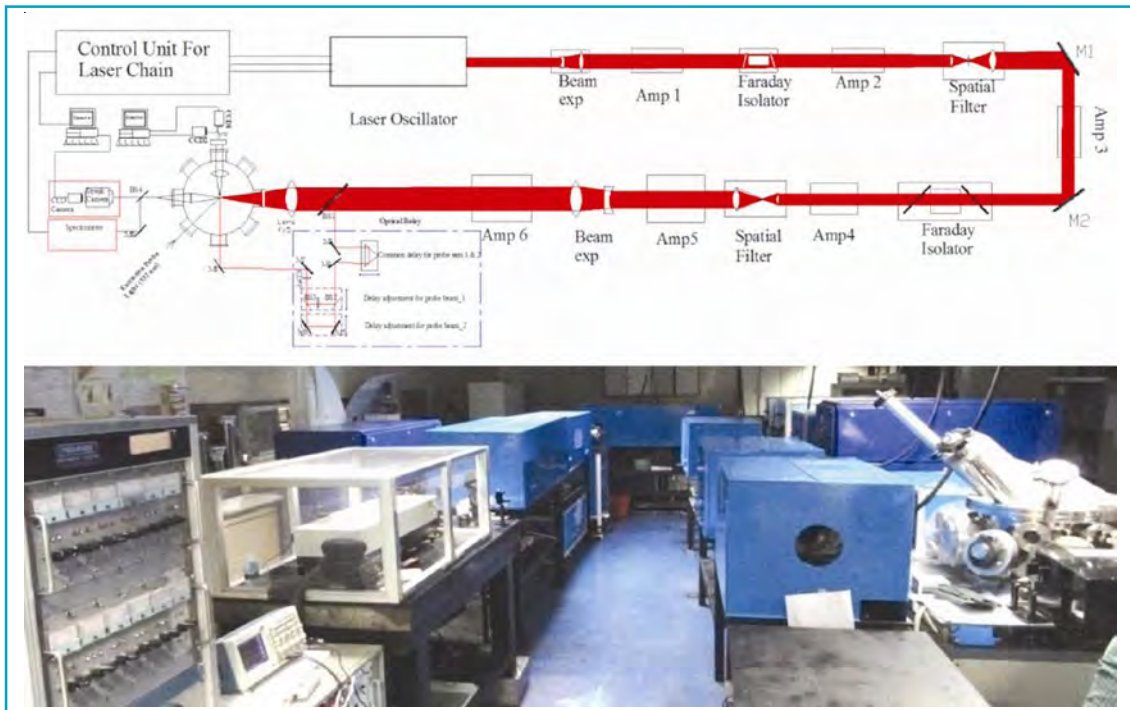


Fig. 1: (a) Schematic and (b) Photograph of the 30 J/300 - 800 ps laser

profile along with the plot of intensity distribution in X and Y axis are shown in Fig. 2. The profile shows a small dip in the center of the beam which is due to radial gain variation occurring in large diameter amplifiers. This was verified by the radial gain variation measurement shown in Fig. 3. The radial gain variation arises due to non-uniform gain

profile across large diameter amplifiers. The gain at different radial points was measured for different electrical input energy to the amplifier as well as the energy of the probe beam. It was found that the radial gain variation was between 12-15% which is very much admissible in a large aperture amplifier; this effect was evident in the final laser beam profile

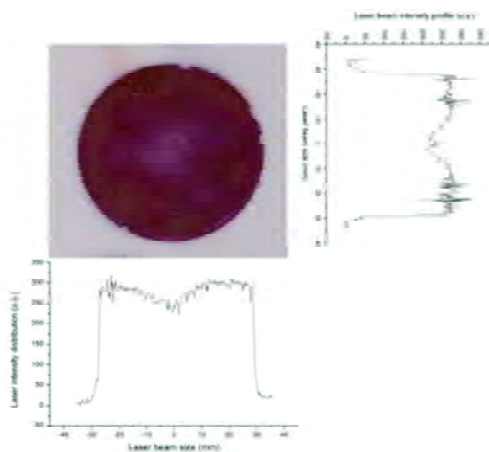


Fig. 2: Final laser beam profile and intensity distribution plot along the X- axis and Y-axis of 30 J laser pulse at the experimental chamber

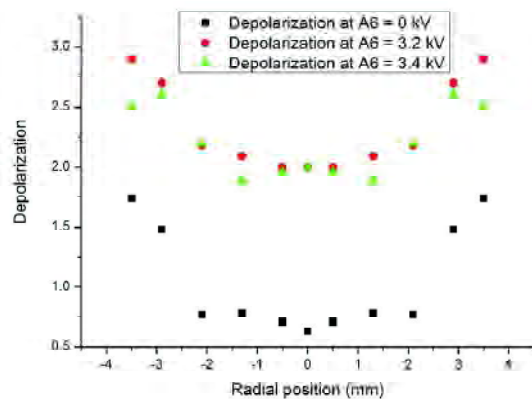


Fig. 3: Radial gain variation of 75 mm diameter Nd:Glass amplifier at 18.5 kJ (red) and 20.8 kJ (black) electrical input energies

shown in Fig. 2. The radial gain profile measurement for electrical input energies of 18.5 kJ and 20.8 kJ are shown in Fig. 3. The scaling of single pass amplifier gain with respect to electrical input energy was also studied for various probe beam energies. For an electrical input energy of 20.8 kJ, the A6 amplifier yielded a single pass gain of 1.6. Another problem faced by high power amplifiers is thermal depolarization due to generation of heat caused by various reasons like: (a) Quantum defect, which is photon energy loss to the host lattice, (b) Non-radiative relaxations from the upper laser level to the ground state and (c) in flash lamp-pumped systems, the broad spectral distribution of the pump source causes a certain amount of background absorption, particularly in the ultraviolet and infrared regions, there by heating the host material. The optical distortion in single-shot lasers arises from thermal gradients produced during the pump cycle. The study of thermally induced depolarization measurement in 75 mm amplifier was done by measuring the percentage depolarization of a laser beam passing through it during flash lamp pumping. A cooling interval of 15 minutes was maintained between successive shots. For fixed probe beam energy, the depolarization was measured for different electrical input energies. The depolarization was found to be 3-4 % when pumped with 18.5 kJ of electrical input energy with only a slight increase at 20.8 kJ of electrical input energy as shown in Fig. 4.

Laser electronics

In the laser power supply each pair of flash lamp is charged by a 400 μF capacitor bank which can be formed either in (100 μF x 4) or (200 μF x 2) network. A comparative study of flash lamp current profile carried out with each configuration revealed that flash lamp profile did not show much variation other than a marginal increase in pulse rise time and the pulse duration in case of 200 μF x 2 network, due to its increased equivalent series inductance (ESL). We have opted for 200 μF x 2 network as it reduces the number of capacitors used and is compact. All

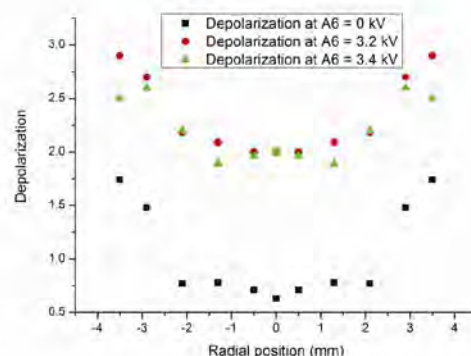


Fig. 4: Effect of electrical input energy on the depolarization of optical laser energy along the rod diameter.

control circuits were modified to accommodate the extra capacitor bank (400 μF each for additional lamp pair) in all power supplies. During the operation of laser chain, the capacitors that are initially charged to a voltage of 3.5kV discharge through the entire flash lamp system (66 flash lamps in 6 amplification stages) dumping more than 80 kJ of electrical energy in the system within pulse duration of 600 microseconds. The low impedance of flash lamps at the peak of discharge process results in an enormous current flow (kA) through them. This high current in short duration generated high levels of Electromagnetic interference (EMI) creating electrical disturbance in the synchronization unit leading to frequent misfiring of laser system. The EMI related problems are solved to a great extent by providing shielded enclosures and special low impedance groundings to circuits and by replacing the existing hard wired control system with a newly developed ARM microcontroller based control unit. Proper isolation is provided via opto-coupler at various stages of the synchronization circuit. The BNC cables used in the transmission and receiver circuits are also replaced with optical fiber cables to prevent EMI. The schematic of the laser electronics is shown in Fig. 5.

Experimental set up

The schematic of experimental set up and photograph of the experimental chamber are shown in Fig. 1a and Fig. 6 respectively. The Gaussian

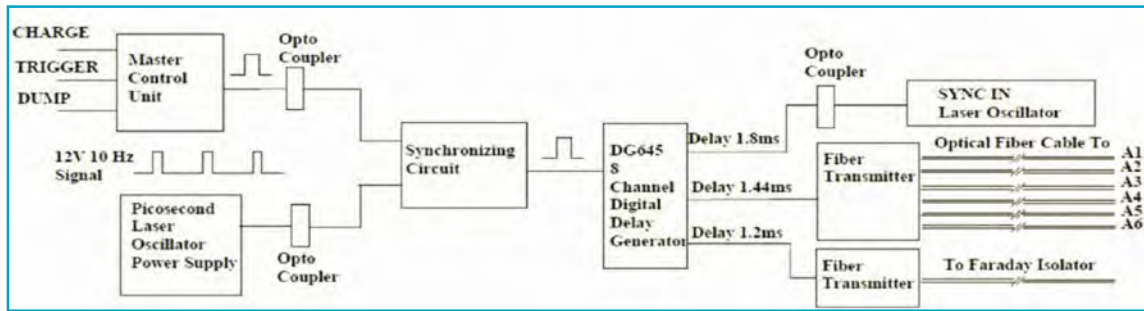


Fig. 5: Schematic diagram of the synchronization circuit of the 30 J laser system.

shaped laser pulse was focused normally on the target foils to a spot diameter of 100 - 150 μm yielding intensity up to $1 \times 10^{15} \text{ W/cm}^2$. The targets are placed in the vacuum chamber evacuated to 2×10^{-6} mbar pressures. More than fifteen plasma diagnostics have been developed for ion, x-ray emission characterization and laser driven shock studies.



Fig. 6: Photograph of experimental chamber. Red line shows path of the main laser beam in the chamber.

and 500 ps respectively was used to measure the foil's free surface displacement at various time delays, from which the free surface velocity (u_s) and hence particle velocity, u_p where $u_p = u_s/2$ were calculated².

The scaling of particle velocity of foil was determined for laser intensities ranging from $6 \times 10^{13} \text{ W/cm}^2$ to $3 \times 10^{14} \text{ W/cm}^2$ and was observed as $u_p = I^\alpha$, where $\alpha = 0.85$. The shock velocity (u_s) and shock pressure (P) were calculated using standard equation of state relations $u_s = a + bu_p$ and $P - P_0 = \rho_0 u_s u_p$, where the values of density, ρ_0 and constants (a, b) for PVA are 1.26 g/cc, and 0.246, 1.565 respectively. The scaling of shock pressure with laser intensities along with the published work of others (S. X. Hu et al, Phys. Rev. Lett. 100, 185003 (2008) and Eliezer et al, Phys. Lett. 86A, 464 (1981)) is presented in Fig. 7a. Our results are fairly in agreement with their results. Fig. 7b shows the comparison of P- u_p

(a) Shock pressure measurements in Polyvinyl alcohol (PVA) films using multi-frame optical shadowgraphy

Laser driven shock experiment in the PVA foil was done with the help of multi-frame optical shadowgraph technique. In this experiment, a high sensitive shadowgraph with a magnification of ~ 3.45 and spatial and temporal resolutions of 12 μm

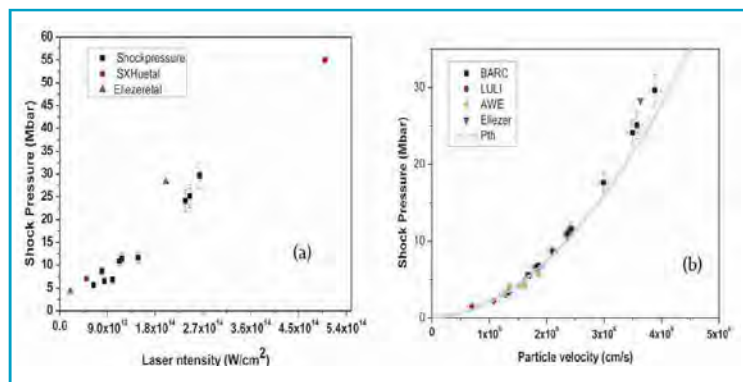


Fig. 7: (a) Scaling of shock pressure with incident laser intensity. (b) The experimental Hugoniot EOS data points for PVA (■) in our experiments, Koenig et al, LULI (●), HELEN, AWE (▲) and Eliezer et al (▼) show good agreement with SESAME curve (—)

Table 1: The values of free surface velocity, particle velocity, shock velocity, and pressure are prepared with shadowgraph record

(Thickness) Targets	Free surface velocity (x 10 ⁶ cm/s)	Particle velocity (x 10 ⁶ cm/s)	Shock velocity (x 10 ⁶ cm/s)	Pressure (Mbar)
5 μm Al	3.599	1.7995	2.95	14.33
5 μm Al	3.75	1.875	3.04	15.36
5 μm Al	3.47	1.735	2.855	13.34
15 μm PVA	6.3	3.15	5.19	20.5
(15 + 5 μm) PVA + Al	4.799	2.4	3.752	24.31
(15 + 5 μm) PVA + Al	4.88	2.44	3.8057	25.1

Hugoniot curve generated by our experimental data with the results of previous experimental and theoretical studies by Koenig at LULI, data from HELEN, AWE, UK and Eliezer. These results are also found to be in agreement with the theoretical data available in the LASL data book (SESAME data). The maximum pressure attained in the experiment was 30 Mbar, at a laser intensity of $2.7 \times 10^{14} \text{ W/cm}^2$.

(b) Shock Pressure enhancement in Aluminium target coated with low Z ablator (PVA):

In laser driven shock experiments, the shock pressure (P) scales with laser intensity (I) as $P = 8.6 (I / 10^{14})^{2/3} \lambda^{-2/3}$, where λ is laser wavelength; while the hot electron temperature (T_H) scales as $[T_H \propto (I \lambda^2)^\alpha]$, where $\alpha \sim 1/3$ to $2/3$. Therefore, attempts to enhance the shock pressure by increasing laser intensity will also result in the preheating of target by hot electrons. To avoid preheating of foils, the Impedance mismatch technique was used, which delivered enhanced shock pressures at relatively low laser intensities. The study of laser driven shock in 5 μm Al and 5 μm Al coated with 15 μm PVA (Low Z ablator) is presented³. The shock and particle velocities were measured using optical streak camera and optical shadowgraph respectively. The shock pressure was then calculated independently from streak

camera data and shadowgraphy data using the EOS relation mentioned earlier with values of a, b and ρ_0 for the Aluminum as 0.5386, 1.339 and 2.7g/cc and that for PVA as 0.246, 1.565 and 1.26g/cc respectively. The particle velocity (free surface velocity), shock velocity and shock pressure for the 5 μm Al, 15 μm PVA and 5 μm Al coated with 15 μm PVA are given in Table 1. From the table it is clear that at fixed laser intensity, the pressure increased by ~1.69 times in Al + PVA layered target (24.31 Mbar) compared to single Al foil (14.33 Mbar). Similar results were obtained from the streak camera records. In this case amplification of 1.67 to 1.71 was measured.

To verify our results, simulations were performed using the one-dimensional radiation-hydrodynamics simulation code HYADES⁴. The simulation results

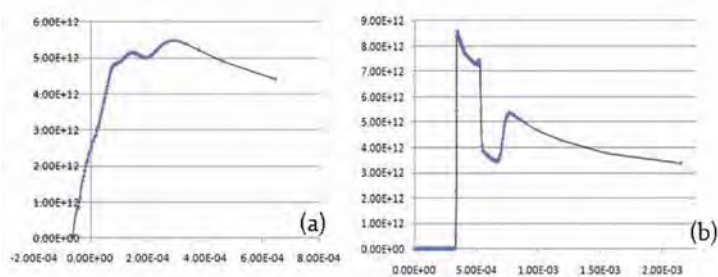


Fig. 8: Theoretical simulation done using HYADES code at laser intensity $6 \times 10^{13} \text{ W/cm}^2$ (10 J, 500 ps, focal spot diameter ~200 μm) for the shock pressure calculation in (a) 5 μm thick Al foil and (b) 15 μm thick PVA + 5 μm thick Al foil.

are shown in Figs. 8a & 8b. The simulation was done for laser energy 10 J in 500 ps pulse duration focussed on the target in 200 μm spot size. From the figure it is clear that the shock pressure in 5 μm Al and 15 μm PVA + 5 μm Al are 5 -5.5 and 8.5 – 9.25 Mbar respectively. From the simulation results also, we observed shock pressure multiplication of 1.68 – 1.72 in 5 μm Al foil coated with 15 μm PVA when compared to plain 5 μm Al foil.

(c) Suppression of instability by double ablation in tungsten doped low Z ablator foils

In laser driven shock experiments, R-T instability, existing due to non uniformities in the target and laser imprint, results in an exponential growth ($e^{\gamma t}$) of any small perturbations in the ablation surface causing density variations in the foil leading to its fragmentation. The instability growth factor is given by $\gamma = \sqrt{kg/1+kL} - \beta kv_a$, where k is perturbation wave number, g is foil acceleration, L is plasma density scale length at the ablation surface, β is numerical coefficient determining the effectiveness of the ablation effect, and v_a is ablation velocity. To mitigate RT instability Fujioka (Phys. Rev. Let. 92, 195001, 2004) proposed the concept of Double Ablation in which plastic targets doped with high Z elements are used. Our studies⁵ on RT

instability suppression were performed with PVA and Tungsten (W) doped PVA targets. The shadowgrams of PVA and PVA (W) given in Fig. 9a-h evidently show stable accelerations of doped foils up to 8 ns. The flyer velocity of doped foils also increased to more than twice when compared to plain PVA foils for laser intensities in the range of $3 \times 10^{13} \text{ W/cm}^2$ - $9.6 \times 10^{13} \text{ W/cm}^2$. The soft X-ray ($> 0.9 \text{ keV}$) yield from doped targets were on an average 3.7 times higher than that from un-doped targets, while enhancement in hard X-ray (3 - 5 keV) was more than 6.7 times. This enhanced X-ray emission in PVA (W) targets is responsible for the creation of radiation driven ablation (RA) front ahead of electron driven ablation (EA) front leading to longer density scale length (L) as well as higher ablation velocity (v_a) therefore thermally smoothing out any non uniformity in laser imprint being coupled to the RA front. From the above equation, we can see that the instability growth factor γ is reduced when density scale length and ablation velocity increases resulting in stable acceleration in doped PVA foils.

Conclusion

A 30 J/ 300 - 800 ps (focusable intensity $\sim 1 \times 10^{15} \text{ W/cm}^2$) Nd: Glass laser system was indigenously developed at HP&SRPD. Several experiments on the laser driven shock and related phenomena such as

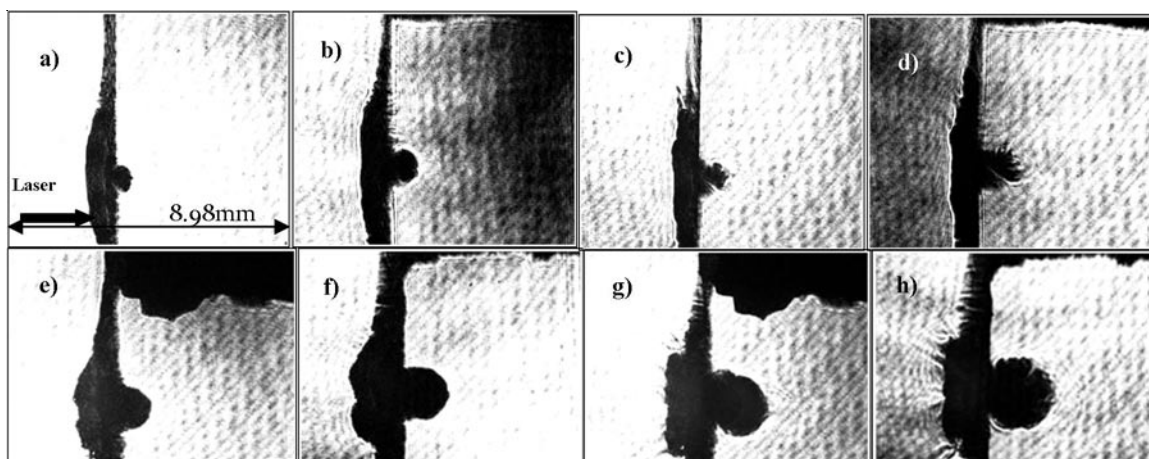


Fig. 9: Shadowgraph records of "foil" free surface (flyer) movement at time delays of 2.92, 4.82, 6.39 and 8.29 ns after laser irradiation at laser intensity of $8 \times 10^{13} \text{ W/cm}^2$. 9(a)-(d) shows the 15 μm "PVA" free surface movement. 9(e) - (f) shows 15 μm Tungsten doped "PVA" free surface movement

preheating and R-T instability were conducted. A maximum shock pressure of 30 Mbar was measured in the PVA target by direct laser ablation, attained with a laser intensity of 2.7×10^{14} W/cm². Experiments with layered targets using impedance mismatch technique was performed to overcome preheating and shock multiplication of 1.69 to 1.75 was observed when 5 μ m Al target was coated with 15 μ m PVA layer. Studies on high Z element doped plastic targets revealed suppression of instability during the acceleration of foils resulting in stable and enhanced flyer foil velocity almost 2 times higher for doped foils than undoped foils. The experimental results were compared with the theoretical simulations and found to be closely matching with the theoretical results.

Acknowledgement

The authors wish to acknowledge Dr. S. M. Sharma, Associate Director, Physics Group & Head, HP&SRPD for his consistent support and encouragement. The authors also wish to acknowledge the excellent support provided by Shri S. K. Lalwani, Electronics Division, BARC and Shri M. S. Ansari, Laser Electronics Support Division, RRCAT, for modifying the electronics and for the mitigation of Electromagnetic Interference. Authors wish to

acknowledge Dr Manmohan Kumar, RPCD, BARC for providing some of the targets and Dr John Pasley, University of York for providing theoretical support on shock experiments. Authors also wish to acknowledge the team from TSD for providing special grounding in the lab.

References

1. Science on High Energy Lasers: From today to the NIF, R. W. Lee, R. Petrasso, R. W. Falcone, UCRL ID 119170 (1995)
2. S. Chaurasia, S. Tripathi, P. Leshma, J. Pasley and M. Kumar, "Shock pressure measurements in polyvinyl alcohol (PVA) films using multi-frame optical shadowgraphy", *Journal of Physics* **377** (2012): 012042.
3. S. Chaurasia, P. Leshma, J. Pasley, S. Tripathi and M. Kumar, "Shock pressure multiplication in layered PVA + Al targets driven by a high-power laser pulse", *Current Science* **103** (2012): 1447.
4. T. Larsen and S. M. Lane, "HYADES—A plasma hydrodynamics code for dense plasma studies", *J. Quantitative Spectroscopy and Radiative Transfer* **51** (1994): 179.
5. P. Leshma and S. Chaurasia, "Suppression of instability by double ablation in tungsten doped polyvinyl alcohol foils", *Journal of Physics* **377** (2012): 012050.

Diagnostic & Prognostic System for Identification of Accident Scenarios and Prediction of “Source Term” in Nuclear Power Plants under Accident Conditions

Santhosh, B. Gera, Mithilesh Kumar, I. Thangamani, M. Hari Prasad, A. Srivastava, Anu Dutta, Pavan K. Sharma, P. Majumdar, V. Verma, Sunil Ganju, V. Gopika, B. Chatterjee, R.K. Singh, K.K. Vaze and A.K. Ghosh
Reactor Safety Division

Abstract

Nuclear power plant experiences a number of transients during its operations. These transients may be due to equipment failure, malfunctioning of process support systems etc. In such a situation, the plant may result in an abnormal state which is undesired. In case of such an undesired plant condition, the operator has to carry out diagnostic and corrective actions. When an event occurs starting from the steady state operation, instruments' readings develop a time dependent pattern and these patterns are unique with respect to the type of the particular event. Therefore, by properly selecting the plant process parameters, the transients can be distinguished. In this connection, a computer based tool known as Diagnostic and Prognostic System has been developed for identification of large pipe break scenarios in 220 MWe Pressurised Heavy Water Reactors (PHWRs) and for prediction of expected “Source Term” and consequence for a situation where Emergency Core Cooling System (ECCS) is not available or partially available. Diagnostic and Prognostic System is essentially a transient identification and expected source term forecasting system. The system is based on Artificial Neural Networks (ANNs) that continuously monitors the plant conditions and identifies a Loss Of Coolant Accident (LOCA) scenario quickly based on the reactor process parameter values. The system further identifies the availability of injection of ECCS and in case non-availability of ECCS, it can forecast expected “Source Term”. The system is a support to plant operators as well as for emergency preparedness. The ANN is trained with a process parameter database pertaining to accident conditions and tested against blind exercises. In order to see the feasibility of implementing in the plant for real-time diagnosis, this system has been set up on a high speed computing facility and has been demonstrated successfully for LOCA scenarios.

Introduction

Nuclear power plants are highly complex systems that are operated and monitored by human operators. When faced with an unplanned transient, such as a plant accident scenario, equipment failure or an external disturbance to the system, the operator has to carry out the diagnostic and corrective actions based on the process instrument readings. Depending upon the severity of an accident, instruments' readings might not give a clear indication of an anomaly at its incipient stage. Therefore, it necessitates developing an intelligent system that will assist the operator to identify such

transients at the earliest stages of their developments. The objective of the plant diagnostic system in any potentially unsafe scenario is to give the plant operators appropriate inputs to formulate, confirm, initiate and perform the corrective actions [1]. Analysis of an event involves determination of the consequence of a specified event such as loss of coolant accident (LOCA) in terms of fuel temperature, storage tank level, containment temperature and pressure and releases, if any. Diagnosis is the identification of the event from the instrumented signals. For this purpose; a

methodology has been developed which consists of database of the above mentioned process parameters. An artificial neural network based diagnostic system has been developed to diagnose the initiating events (IEs) of a typical Indian PHWR from the process parameters available in the computerised operator information system (COIS). To train the network; a large database of these parameters has been generated. The break scenarios have been modeled with a single neural network consisting of 37 inputs, 3 outputs and 2 layers of hidden neurons. Among the list of many process parameters available in the COIS [2], 35 parameters such as south inlet header pressure, south outlet header pressure, D₂O storage tank level, pump room pressure, reactor power, etc. are found to be significant for LOCA identification and have been selected for diagnosis. The time-dependent transient data pertaining to the reactor core and containment generated through Multi Step and Multi Physics (MSMP) approach forms the data base [3]. The ANN is trained with a process parameter data base pertaining to Large break LOCA (LBLOCA) scenarios as well as LBLOCA with Loss of ECCS. The data base covers various break sizes (20-200% of Reactor Inlet Header (RIH) cross-section) and breaks at different header locations. The training and testing of neural networks were carried out using BIKAS neural networks simulator [4] using the data base. The results obtained from the study are satisfactory and currently will be helpful in the accident management of Nuclear Power Plants (NPPs). Technical feasibility of the system is assessed by implementing the system on a high speed computing facility to demonstrate successfully LOCA scenarios. Whenever an event is identified, this system will display the type of the event, time at which the event has occurred, relevant process parameters and their values at the time of initiation of the event and necessary operator actions.

Brief description of Indian PHWR

The Primary Heat Transport (PHT) system of 220 MWe Indian PHWRs is shown in Fig. 1. It is in the

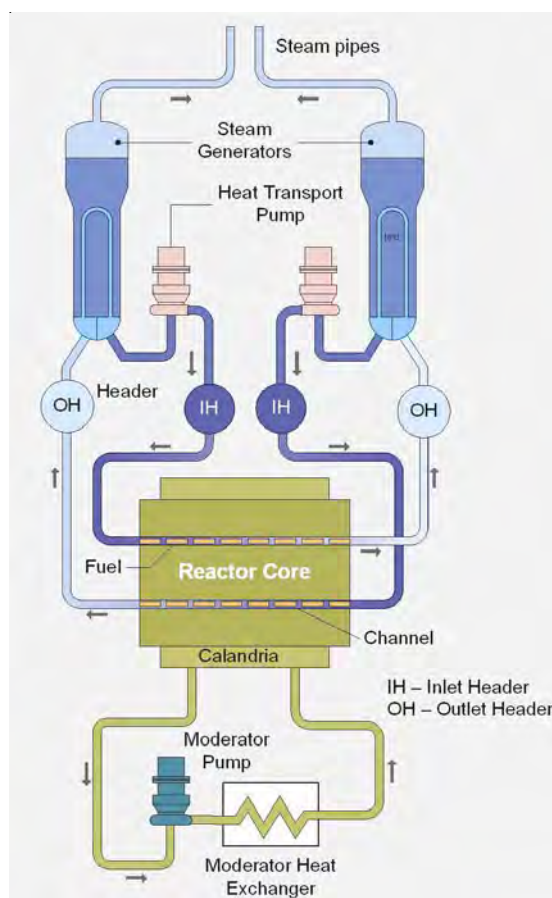


Fig. 1: PHT system of Indian PHWR

shape of a “Figure of Eight” with each leg having an inlet header providing coolant to half of the channels of the reactor core and an outlet header receiving the hot coolant from the reactor channels. There are 306 horizontal coolant channels in 220 MWe Indian PHWRs. Each channel consists of 12 fuel bundles contained in a pressure tube, which is surrounded by a calandria tube. The annulus between the pressure tube and the calandria tube contains gas, which provides the required thermal insulation under normal operating conditions. The calandria tube is submerged in the relatively cold heavy water moderator. The primary coolant flows inside the pressure tube containing the 19-rod fuel bundle. Auxiliary system like feed and bleed system helps to maintain the system inventory and the pressure and is achieved with the help of PHT storage tank, bleed condenser and pressurizing pump. The reactor is equipped with ECCS with heavy water and light

water hydro accumulators along with long term pumped recirculation system. ECCS is designed to limit the consequences of events such as LOCA. Indian PHWR has two shutdown systems namely, primary shutdown system and secondary shutdown system to bring the reactor to shutdown state.

The Indian PHWR of the current design has a double containment with a vapour suppression pool. The inner Primary Containment (PC) is surrounded by outer Secondary Containment (SC) and equipped with containment Engineered Safety Features (ESFs) like charcoal and High Efficiency Particulate Air (HEPA) filters with containment coolers and blowers. The containment design consideration includes energy deposition from LOCA and Main Steam Line Break (MSLB). One of the major objectives of the containment is to limit the release of radioactivity at the ground level as well as through the stack within the permissible limits both during normal operation and under accident conditions.

In the context of design requirements from radioactivity release point of view, the accident scenario considered is a LOCA involving a double ended guillotine rupture of the RIH. The resulting flashing of high enthalpy liquid into the volume V1 will lead to its pressurization. The pressure differential between volumes V1 and V2 causes the water column in the vents to recede (vent clearing). Once the vents are cleared, it establishes the steam-air mixture flow from V1 to V2. The steam-air mixture bubbles through the pool where the steam gets condensed completely and the hot air is cooled before passing to volume V2. The vapour suppression pool performs the important function of energy as well as radionuclide management. As an energy management feature it limits the peak pressure and temperature in the containment following a LOCA by completely condensing the incoming steam. By limiting the peak pressure, the driving force for leakage of Fission Products (FPs) to environment is reduced. Radionuclide management, which is a secondary function of the vapour suppression pool, involves effective FPs removal by

dissolving, trapping, entraining or scrubbing away part of the FPs that reach the pool. All the instrumentation and control parameters pertaining to process and safety systems are continuously displayed on COIS, which is located in reactor control room.

Methodology

Event description

Initiation of break at inlet header leads to a sudden depressurisation of the PHT system. The initial depressurisation rate is found to be high due to initial high subcooled blowdown rate. Within a few milliseconds the pressure falls to the saturation pressure level causing the coolant to flash. The formation of void causes the break discharge rate to be reduced leading to reduction in depressurisation rate. As the break leads to core voiding, the power increases suddenly due to positive coolant void coefficient of the reactor. The peak reactor power is different in different LOCA scenarios. The maximum peak power rises to 1.93 times the initial power in case of 200% break. After the reactor scram, power starts coming down and follow the decay power curve. The variation of quality in different sizes of break is all most similar. In broken pass the fluctuation of quality is very high since this pass is directly connected to broken header. ECCS starts the injection when the pressure in any one of the headers reaches 55 kg/cm² (g). The time of injection and rate of ECCS coolant enters into the channel depends upon the size of the break. Several reactor trip signals will be activated namely high log rate, low PHT pressure, high neutron power, low PHT coolant flow and high reactor building pressure one after the other in a short period of time. Sequence of actuation of trip signals is largely dependent upon the break size and location. In general, for large breaks on RIH side, high log rate signal is the first signal followed by high neutron power, while for breaks on Reactor Outlet Header (ROH) side, low pressure signal is usually the first signal followed by high log rate. In general, it is observed that, larger the break, larger the blowdown

energy discharge and more depressurisation. Hence, early injection of ECCS is possible [5].

Database generation

A Multi Step and Multi Physics (MSMP) approach has been adopted for analysing different cases pertaining to LOCA and LOCA with loss of ECCS. Analysis has been carried out for the following cases of LOCA: (i) Reactor Inlet Header Break with ECCS available (RIHECCS) (ii) Reactor Outlet Header Break with ECCS available (ROHECCS) (iii) Reactor Inlet Header Break without ECCS (RIHNoECCS) (iv) Outlet Header Break without ECCS (ROHNoECCS). Various break sizes ranging from 20% to 200% have been considered in each case mentioned above. In each case, it has been assumed that the reactor has tripped on the first trip signal. The inverse calculation of identifying the event from the symptoms is based on a large ensemble of such signals generated by the following analyses. The flow of information among the system codes to generate the database is shown in Fig. 2. In the first stage, the core thermal-hydraulic response of the plant under an accident is computed, followed by computation of FPs release from the reactor core. This release is based on the fuel temperature transients computed in the first stage and the steady state FP inventory present in the core. In the second stage, FP transport in the primary heat transport system and its release into the containment is computed with the core thermal-hydraulic parameters and FP release parameters computed in stage one and two respectively. In the next stage, containment thermal hydraulic behaviour,

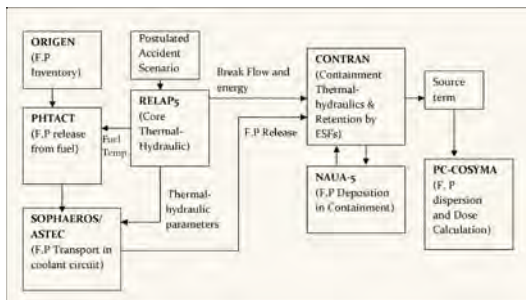


Fig. 2: MSMP approach for database generation and consequence analysis

FP retention by different containment ESFs and deposition are evaluated [5].

To study the system behaviour under large break LOCA condition, a spectrum of break sizes has been analyzed for core and containment. Following are some of the typical process parameters' profiles generated from RELAP5 simulation for a 200% break in RIH with ECCS case. For example, Fig. 3 shows

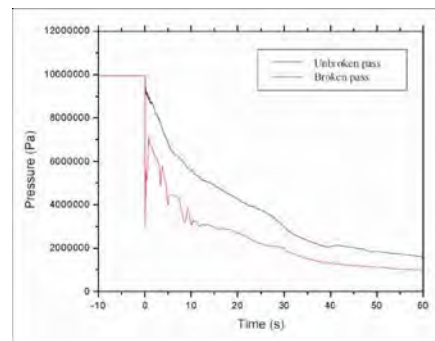


Fig. 3: RIH pressure

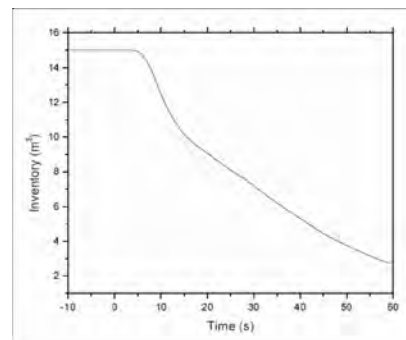


Fig. 4: D₂O inventory in PHT system

the header pressure in the broken and unbroken pass and Fig. 4 shows the D₂O inventory in the PHT system.

Event identification

An artificial neural network based diagnostic system has been developed with the transient data mentioned above for various postulated accident scenarios of LOCA. ANN is an information processing paradigm that is inspired by the way the biological nervous systems, such as the brain, process information [6]. It is a system modeled based on

human brain. ANNs, like humans, learn by examples. It is an attempt to simulate, within specialized hardware or sophisticated software, the multiple layers of neurons [7]. Each neuron is linked to a few of its neighbours with varying coefficients of connectivity that represent the strengths of these connections. Learning is accomplished by adjusting these strengths to cause the overall network to output appropriate results [8]. A general characteristic of a neural network is the ability that quickly recognizes the various conditions or states of a complex system once it has been suitably trained [9]. The functional block diagram of ANN based diagnostic system also

known as symptom based diagnostic system (SBDS)¹ is shown in Fig. 5.

It mainly consists of three stages of processing, namely, the input, output and the event identification stage. In the input stage, the data is taken from the COIS and processed into training and testing files. This data is used for training and testing the neural networks in the event identification stage. In the event identification stage, neural network processes the data through a bank of artificial neuron layers and arrives at an optimum solution by adjusting the synaptic weights. Finally, the diagnostic results obtained in the event identification stage are displayed in the

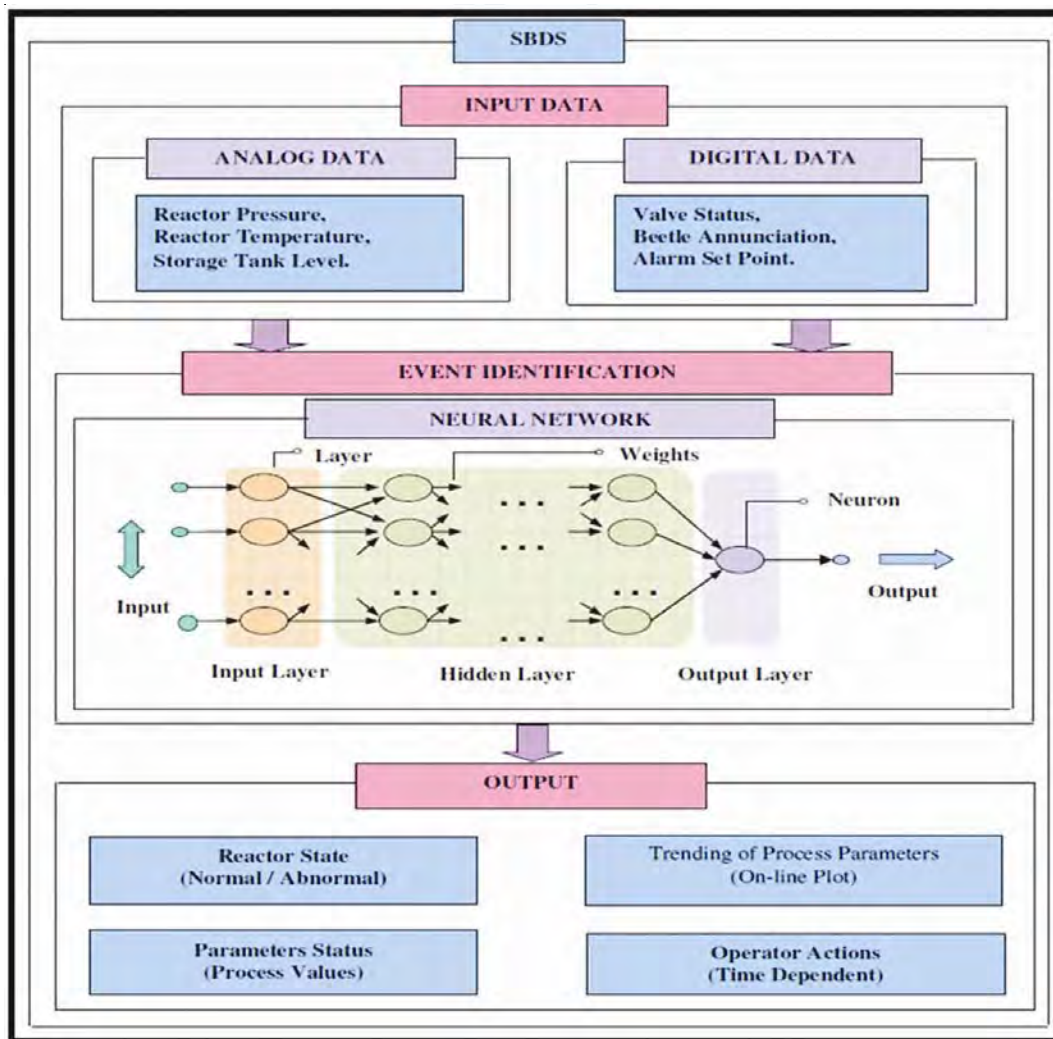


Fig. 5: Functional block diagram of SBDS

Table 1: List of process parameters for LOCA

Sl. No.	Parameter description	Process range
1	South inlet header (CL) pressure CH-G	0 - 120 kg/sq. cm g
2	PHT pressure in south hot header CH-D	55 - 105 kg/sq. cm g
3	North inlet header (CR) pressure CH - G	0 - 120 kg/sq. cm g
4	PHT pressure in north hot header CH-D	55 - 105 kg/sq. cm g
5	ÄP across header HR & CL CH - G	- 75 - 75 cmWC
6	ÄP across header HL & CR CH - G	- 75 - 75 cmWC
7	D ₂ O storage tank level CH - E	0 - 4 m
8	SG1 inlet temperature	0 - 320 Deg. C
9	SG1 outlet temperature	0 - 320 Deg. C
10	SG2 inlet temperature	0 - 320 Deg. C
11	SG2 outlet temperature	0 - 320 Deg. C
12	SG3 inlet temperature	0 - 320 Deg. C
13	SG3 outlet temperature	0 - 320 Deg. C
14	SG4 inlet temperature	0 - 320 Deg. C
15	SG4 outlet temperature	0 - 320 Deg. C
16	Diff temperature across SG1 CH - E	0 - 55 Deg. C
17	Diff temperature across SG2 CH - E	0 - 55 Deg. C
18	Diff temperature across SG3 CH - A/D	0 - 55 Deg. C
19	Diff temperature across SG4 CH - A/D	0 - 55 Deg. C
20	Steam flow from BO1	0 - 375000 kg/Hr
21	Steam flow from BO2	0 - 375000 kg/Hr
22	Steam flow from BO3	0 - 375000 kg/Hr
23	Steam flow from BO4	0 - 375000 kg/Hr
24	Selected channel N - 13 inlet temp	0 - 300 Deg. C
25	Selected channel N - 13 outlet temp	0 - 300 Deg. C
26	Selected channel H - 18 inlet temp	0 - 300 Deg. C
27	Selected channel H - 18 outlet temp	0 - 300 Deg. C
28	Channel flow south N - 13 CH - D	0 - 51100 kg/Hr
29	Channel flow south H - 18 CH - E	0 - 45200 kg/Hr
30	RB pump room pressure (WR)	0.1 - 5 kg/sq. cm g
31	PHT pump room air temperature	0 - 100 Deg. C
32	D ₂ O level in 3335 - TK1 CH - G	0 - 168 cm
33	H ₂ O level in 3335 - TK3A & 3B CH - G	0 - 3852 mmWC
34	PSS linear N CH - D	0 - 150 %FP
35	PSS log rate CH - D	- 20 - 20 %/sec
36	PHT pump room air temperature	High (Digital)
37	PSS log rate CH - D	Trip (Digital)

output stage, which is an operator screen. In the output stage, following information is displayed: the plant status, i.e., the plant normal or any

transient has occurred, the parameters and their current process values, the trend of the important process parameters and operator actions whenever

an event is detected. In the prediction mode, from the transients recorded in the computerised operator information system, the system predicts the information on LOCA (location and size of break) and status of availability of ECCS. Hence the occurrence of an event such as LOCA can be detected by continuously monitoring the reactor process parameters such as PHT storage tank level, pressure and temperature, steam generator level, containment pressure and temperature, etc. The events are modelled based on the relevant reactor process parameters' time dependent data as available in the COIS. A large amount of time dependent data has been generated in order to train and test the neural networks for the selected scenarios so that these scenarios can be identified during reactor operations [10]. The important process parameters identified from the COIS of a typical Indian PHWRs for the LOCA is shown in Table 1. Only the measurable parameters, which are listed in COIS have been selected for this analysis.

In order to illustrate the developed methodology, large break LOCA in RIH with ECCS is selected. The break sizes considered for this event are 20%, 60%, 75%, 100%, 120%, 160% and 200% of double ended break in RIH. A 60 seconds transient duration is considered under the assumption that this time duration is sufficient to identify a large break LOCA scenario [3,5,10]. To accomplish this task, a neural network consisting of 37 input neurons and 3 output neurons has been selected. A 3-neuron output pattern represents as follows: the first parameter of

the output represents the size of the break (percent of cross-sectional area of RIH), second parameter representing the location of the break (i.e., 0 for RIH and 1 for ROH) and the last parameter representing the status of ECCS (i.e., 0 for without the availability of ECCS and 1 for with the availability of ECCS). Table 2 shows the representation of output neurons for 20% and 60% break cases. A similar representation is followed for remaining break scenarios. The total number of break scenarios is 32 and they are derived as follows; the break sizes are 20%, 40%, 60%, 75%, 100%, 120%, 160% and 200%, each one being in RIH and ROH, and again with and without ECCS thus leading to a total of 32 large break LOCA scenarios. In addition, the normal reactor state is also modelled in the same network.

As discussed earlier, the transient data was generated using RELAP5 and other thermal-hydraulic codes. The number of hidden layers and neurons in each layer were selected based on the following study [11]. First order resilient back propagation with batch mode of training was used. Unipolar sigmoid activation function and sum squared error function were used. The network consisting of 37 input neurons, 3 output neurons, 26 neurons in first and 19 neurons in second hidden layers. The number of neurons in the hidden layers was selected by carrying out a parametric study and choosing the configuration with the minimum error [11]. Training of ANN was carried out on a typical Pentium IV processor with 1.5GHz and 512MB of RAM. The total CPU time the simulator took was approximately 24Hrs to converge to a minimum error of $1.42E-02$ in about 76000 epochs.

Results and Discussion

Table 3 shows the testing results obtained from neural network model. The value of each of the second and third parameters of the output can be either 0 or 1. However, in a floating point arithmetic calculation with the ANN they can assume values other than 0 or 1. For these parameters, calculated values less than 0.5 are regarded as 0 and

Table 2: Output representation

Output pattern	Description
20.0, 0.0, 0.0	20% break in RIH with ECCS
20.0, 0.0, 1.0	20% break in RIH without ECCS
20.0, 1.0, 0.0	20% break in ROH with ECCS
20.0, 1.0, 1.0	20% break in ROH without ECCS
60.0, 0.0, 0.0	60% break in RIH with ECCS
60.0, 0.0, 1.0	60% break in RIH without ECCS
60.0, 1.0, 0.0	60% break in ROH with ECCS
60.0, 1.0, 1.0	60% break in ROH without ECCS

Table 3: Testing results of ANN

Break size (%)	Desired output			Calculated output			RMS error (%)
0	0.0	0.0	0.0	0.2322	-0.0033	-0.1249	0.1523
20	20.0	0.0	0.0	20.95	-0.00497	0.3597	2.34
	20.0	0.0	1.0	19.90	0.0025	0.6459	2.365
	20.0	1.0	0.0	17.21	1.0022	0.0759	3.087
	20.0	1.0	1.0	22.289	0.997	0.995	3.002
60	60.0	0.0	0.0	61.68	-0.00012	0.148	2.912
	60.0	0.0	1.0	59.73	-0.00077	0.8665	3.358
	60.0	1.0	0.0	59.276	0.998	0.0038	2.712
	60.0	1.0	1.0	56.70	0.999	0.983	3.105
100	100.0	0.0	0.0	103.37	0.0012	0.1397	3.64
	100.0	0.0	1.0	104.23	-0.0032	0.8558	4.107
	100.0	1.0	0.0	101.37	1.0028	-0.0589	2.907
	100.0	1.0	1.0	101.086	1.00	1.0275	3.974
120	120.0	0.0	0.0	120.17	0.0016	0.1134	3.56
	120.0	0.0	1.0	119.39	-0.00048	0.8451	4.422
	120.0	1.0	0.0	122.64	1.0031	-0.0608	2.971
	120.0	1.0	1.0	122.208	0.997	1.043	4.258
200	200.0	0.0	0.0	197.98	0.00033	0.00212	4.856
	200.0	0.0	1.0	193.49	-0.00066	0.97	4.84
	200.0	1.0	0.0	194.87	0.998	-0.0512	5.733
	200.0	1.0	1.0	194.015	1.00	1.059	5.438

those above 0.5 are regarded as 1. For example, in Table 3, the calculated values of (122.64, 1.0031, -0.0608) in the third case under 120% break will be regarded as (122.64, 1.0, 0) which is very close to the desired output.

Few case studies were carried out with the transients of some selected event scenarios which were not

used for training and testing of the ANN. Table 4 shows the predicted results for these scenarios.

Fig. 5 shows the plot of desired and calculated breaks obtained from a trained network. It can be seen from Fig. 5 that the predicted breaks are in good agreement. Fig. 6 shows the predicted breaks against the RMS error in percentage. From the Fig. 6, it is clear that the RMS error for smaller breaks is less compared to larger breaks. This is because of

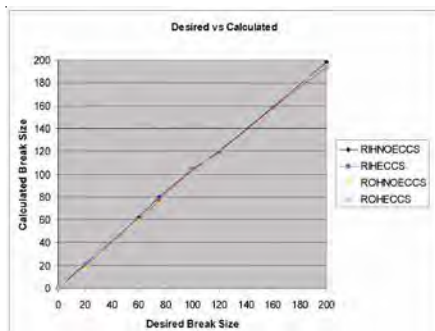


Fig. 5: Desired versus calculated breaks

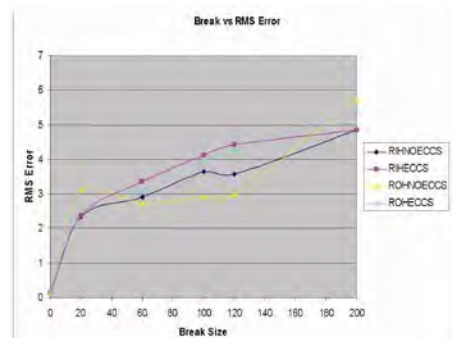


Fig. 6: Predicted breaks versus RMS error (%)

Table 4: Predicted results from a trained network

Break size (%)	Desired output			Predicted output		
40	40.0	0.0	0.0	38.29	0.017	0.15
	40.0	1.0	0.0	38.75	0.99	0.8008
	40.0	1.0	1.0	36.84	0.998	0.878
50	50.0	0.0	0.0	49.27	0.129	0.044
	75	0.0	0.0	79.85	0.00215	0.169
	75	0.0	1.0	77.016	-0.0042	0.862
	75	1.0	0.0	74.014	0.995	-0.064
75	75	1.0	1.0	71.58	0.995	0.985
	160.0	0.0	0.0	158.66	-0.00014	0.040
	160.0	0.0	1.0	158.006	0.00216	0.7765
	160	.160.0	1.0	163.6	1.003	-0.027
160	.160.0	1.0	1.0	164.38	0.996	1.047

the fact that the large break transients are so rapid that many process parameters come almost simultaneously and ANN may not distinguish accurately due to lack of uniqueness in the patterns.

Diagnostic system

Diagnostic system is an intelligent transient identification and operator support system for accident management in nuclear power plants. It identifies the transients quickly by continuously monitoring the reactor process parameters using artificial neural networks. When a transient occurs, instruments' readings develop a time dependent pattern which is unique with respect to the type of transient, its severity and location. This unique time dependent data is used to train neural networks for

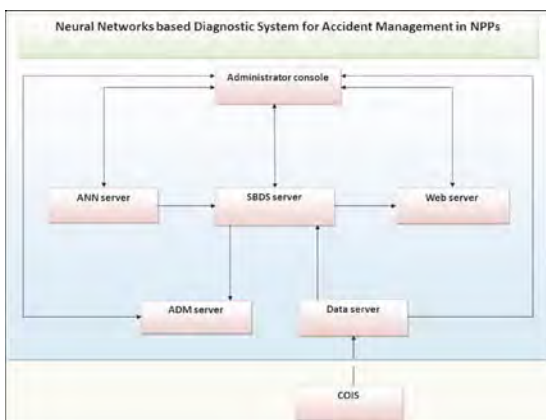


Fig. 7: Architecture of Diagnostic system

future transient prediction. The architecture of the Diagnostic system is shown in Fig. 7. Diagnostic system consists of various remote servers for control and monitoring tasks. Diagnostic system has been set up with a high speed distributed computing servers for fast processing and real-time response, and has been demonstrated successfully



Fig. 8: Diagnostic system setup

for real-time identification of accident scenarios in NPPs.

The setup of Diagnostic system which is installed at Engineering Hall No.3 is shown in Fig. 8. The system has the self-diagnostics which monitors the internal servers and various remote tasks to ensure round-the-clock operation for real-time diagnosis of transients in NPPs.

The administrator console for monitoring various servers and controlling remote tasks is shown in Fig. 9.

Fig. 10 shows a typical output of the Diagnostic system for the identified transient along with the important process parameters and their current process values. The reactor status, type of LOCA

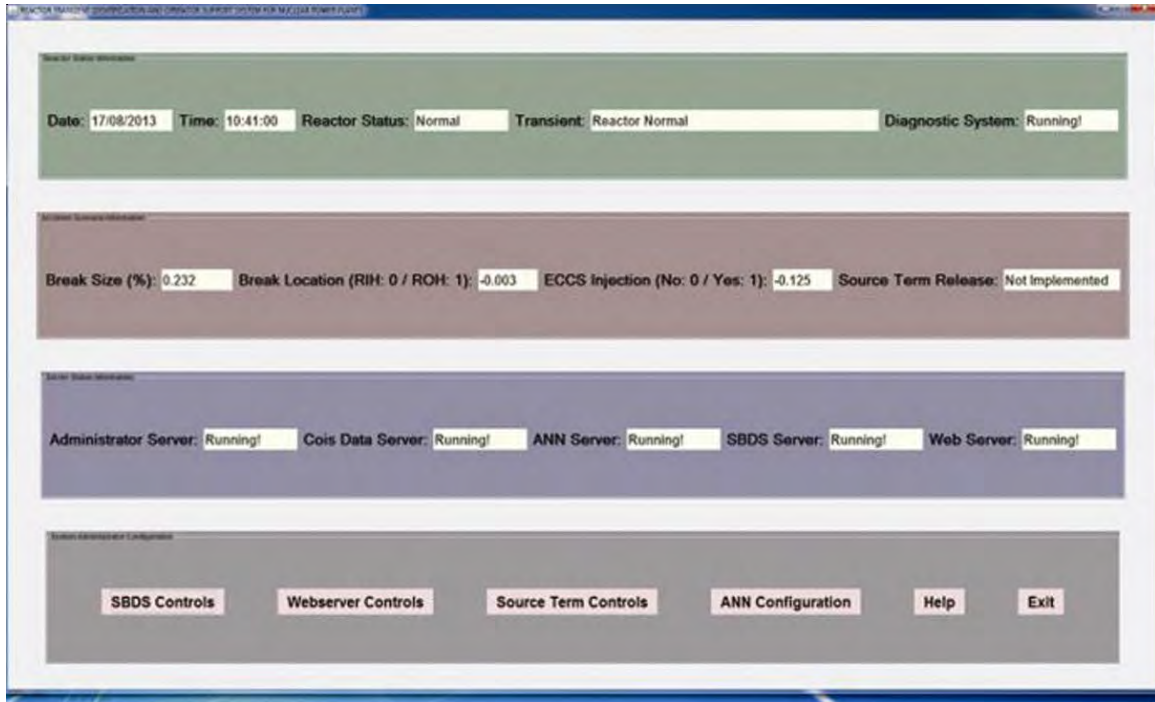


Fig. 9: Administrator console for remote tasks and monitoring



Fig. 10: Diagnostic system output for LOCA scenario

scenario is displayed at the top of the screen. The detected break size, location and availability of ECCS are displayed at the bottom of the screen. Operator actions, whenever an event is identified, will be displayed on the operator screen for the identified transient. The most relevant parameters are highlighted when they cross certain set limits.

Prognostic features in the Diagnostic System

Core Damage phase- Radioactivity release into the containment

Diagnostic system is backed up by the database developed for detailed modeling of core and containment based on MSMP approach for fission product transport from core and containment to environment through leakage path. Hence it is able to predict the possible source term release for 220MWe PHWR in a real time fashion, considering the availability of various containment engineered safety features. This feature will help to provide **ALERT** for emergency preparedness in case of any abnormal conditions.

Post release phase – Radioactivity release into Exclusion Zone

During the nuclear power plant operations, there can be aerial releases of radionuclides. These radionuclides get carried away by the wind and dispersed in the air due to the turbulence. Such released radionuclides introduce doses to the surrounding areas. Correct knowledge of these releases is very much essential for not only emergency preparedness programs but also to limit the doses to the public in the vicinity of the plant. There are environmental radiation monitors installed around the exclusion zone of the NPP to monitor the radiation in the environment due to such releases. Usually the releases from the plant are in controlled manner and monitored continuously. However, in case of accidental release, the above

mentioned quantities may be specific to a particular accident scenario. Therefore, correct estimation of the release during accident conditions is very important for taking appropriate measures for emergency preparedness.

Data from environmental radiation monitors (ERMs) in Radiation Data Acquisition System (RADAS) provide vital information on radiation dose at a particular place around the reactor. Using various computational techniques such as Kalman filter it is possible to predict the release rate and release height for a particular accident scenario. This release information can further be used to estimate the dose rates around the reactor using standard dispersion techniques such as the one commonly used Gaussian plume dispersion model. The dose profile, thus generated, provide an assessment of dispersion pattern and in turn assist in decision making regarding the emergency preparedness. The release evaluations for the detected accident scenario were computed from the Diagnostic system and the geographical dispersion of the radioactivity plume are shown on the operator screen in a real-time manner. Fig. 11 displays the radioactivity profile generated by diagnostic system for the display of atmospheric dispersion of radionuclides.



Fig.11 : Radioactivity plume dispersion using Kalman filter

Conclusions

In this study, several scenarios of large break LOCA with and without the availability of ECCS have been modelled for a standard 220 MWe PHWR using artificial neural networks. The LOCA in RIH with ECCS, RIH without ECCS, and ROH with and without ECCS scenarios have been analyzed. The break sizes ranging from 20% to 200% in reactor headers are considered. A few break sizes were predicted without being trained earlier. The errors in the test results obtained from ANN are quite small. The error in prediction in ranges with sparse data for training is somewhat higher. However, this can be corrected by training with a larger data set. In order to see the feasibility of implementing in the plant for real-time diagnosis, Diagnostic system has been set up on a high speed computing facility and demonstrated successfully for LOCA scenarios. Whenever an event is identified, this system will display the type of the event, time at which the event has occurred, relevant process parameters and their values at the time of initiation of the event and necessary operator actions. Currently, validation exercises are being conducted on this tool to test its prediction capability from plant simulator data. The proposed system would be useful for accident management in nuclear power plants, especially to augment the requirements of Disaster management.

References

1. Santosh, G. Vinod, A. K. Babar, H. S. Kushwaha and V. Venkat Raj, "Symptom based diagnostic system for nuclear power plant operations using artificial neural networks", *Reliability Engineering and System Safety*, Vol. 82, 2002.
2. COIS, Computerized Operator Information System, Kaiga 3 & 4, NPCIL.
3. B. Gera, Mithilesh Kumar, I. Thangamani, H. Prasad, A. Srivastava, P. Majumdar, Anu Dutta, V. Verma, S. Ganju, B. Chatterjee, H.G. Lele, V.V.S.S. Rao, A.K. Ghosh, "Estimation of source term and related consequences for some postulated severe accident scenarios of Indian PHWR", *Nuclear Engineering and Design*, Volume 240, Issue 10, October 2010, Pages 3529-3538
4. BIKAS, Neural Networks Simulator, Version 7.0.5, 2005, BARC.
5. Santosh, B. Gera, Mithilesh Kumar, I. Thangamani, Hari Prasad, A. Srivastava, Anu Dutta, Pavan K. Sharma, P. Majumdar, V. Verma, D. Mukhopadhyay, Sunil Ganju, B. Chatterjee, V.V.S. Sanyasi Rao, H.G. Lele and A.K. Ghosh "Development of a diagnostic system for identifying accident conditions in a reactor", Summary Report, BARC/2009/E/013, BARC, 2009.
6. Barlett E. B., Uhrig R. E., Nuclear Power Plant Status Diagnostics using an Artificial Neural Network, *Nuclear Technology*, Vol. 97, March 1992.
7. Yair Bartal, Jie Lin and Robert E. Uhrig, Nuclear Power Plant Transient Diagnostics using Artificial Neural Networks that allow "Don't Know" classifications, *Nuclear Technology*, Vol. 110, June 1995.
8. Se Woo Cheon and Soon Heung Chang, "Application of neural networks to a connectionist expert system for transient identification in nuclear power plants", *Nuclear Technology*, Vol. 102, May 1993.
9. Yukiharu Ohga and Hiroshi Seki, "Abnormal event identification in nuclear power plants using a neural network and knowledge processing", *Nuclear Technology*, Vol. 101, Feb. 1993.
10. T.V. Santosh, A. Shrivastava, V.V.S. Sanyasi Rao, A.K. Ghosh and H.S. Kushwaha, "Diagnostic System for Identification of Accident Scenarios in Nuclear Power Plants using Artificial Neural Networks" *Reliability Engineering and System Safety*, pp. 759-762, vol.54, 2009.
11. Santosh, Gopika Vinod, R.K. Saraf, A.K. Ghosh and H.S. Kushwaha, "Application of artificial neural networks to nuclear power plant transient diagnosis", *Reliability Engineering and System Safety*, Vol. 92, pp.1486-1472, 2007.

Design and development of an integrated Environmental Radiation Monitor - Automatic Weather Station (ERM-AWS)

A. Vinod Kumar, M.P. Ratheesh, S.S. Salunkhe, R. Jana, S.G. Gavas,
T. Mukundan, P.R. Ninawe, M.S. Prakasha,
S. Garg and M.D. Patel
Radiation Safety Systems Division

Abstract

Online monitoring of atmospheric gamma radiation and meteorological parameters is an important and useful input for handling any radiation emergency. Radiological Safety Systems Division, Bhabha Atomic Research Centre has been developing wide variety of radiation detectors, with continuous improvements based on the advancement in technology and user's requirements. BARC and ISRO (Indian Space Research Organization) under a collaborative program designed and integrated Environmental Radiation Monitor (ERM, developed under IERMON program by BARC) with Automatic Weather Station (AWS, developed by ISRO), as a single stand-alone ERM-AWS system. The system operates with solar powered battery backup and the data transmission is via satellite. ERM-AWS units have been produced and installed at few DAE and non-DAE facilities. A dedicated stand-alone satellite Earth Station has also been established at CTCRS, Anushaktinagar, Mumbai, to receive the data transmitted from ERM-AWS system.

Introduction

BARC as a part of the national level emergency preparedness program is involved in the design and development of standalone solar power based environmental radiation monitors (ERMs) with GSM (Global System for Mobile) communication devices (Patel et al, 2011) and is in the process of expanding the program to country wide network for providing real-time data from stations spread all over the country. ISRO has developed stand alone solar power based Automatic Weather Station (AWS) for measuring various meteorological parameters along with satellite based communication system under the Disaster Management Support and Village Resource Centre Program (Manikiam and Murthy, 2008). Simultaneous measurement and communication of meteorological and radiation data is required for predicting the likely emission source release rate and the forecasting of plume dispersion, in case of an accidental scenario (Vinod Kumar et al., 2008). Keeping in view of this requirement, an integrated ERM-AWS system has been designed and developed jointly by BARC and ISRO.

Secured data transmission and reception facility for ERM-AWS is established through dedicated satellite receptor and transmission system (Garg et al., 2011) for uninterrupted communication of both meteorological and radiation data simultaneously from geospatial locations to centrally located Earth Station for all nuclear installations in India.

The ERM-AWS System details

The ERM-AWS system has a central pole of 7 m height with sensors at various heights. The pole is supported by guy wires. Each ERM-AWS system is having sensors for Wind Speed; Wind Direction; Air Temperature; Humidity; Rainfall; Earth's Net Radiation; Atmospheric Pressure and Environmental Gamma Radiation as shown in Fig. 1. A detailed description of the AWS system and its sensors are given in Manikiam and Murthy, 2008, and details of ERM system are given in Patel et al., 2011. A brief description of these sensors is given below :

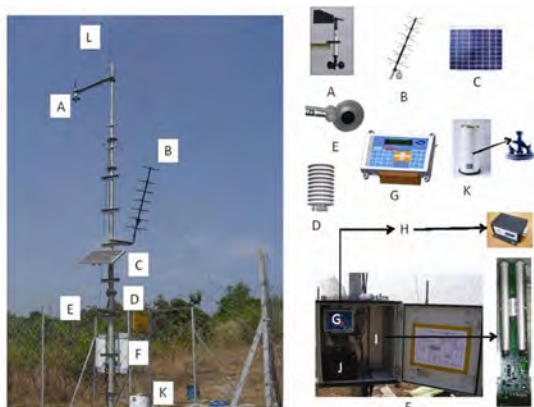


Fig. 1: Installed Integrated ERM-AWS system (A = Wind Vane and Cup Anemometer; B = Transmitting Antenna; C = Solar Panel; D = Temperature & Humidity sensors; E=Net Radiometer, F = Weatherproof Box containing Data Logger (G), Pressure sensor (H), Gamma Radiation Monitor (I), and Battery (J); K = Rain Gauge and L = Lightning Arrester

(a) **Wind sensor** computes instantaneous and average wind speed and two-dimensional direction in the horizontal plane at the level of installation. Wind speed and wind directions are two vital parameters to dictate air mass and airborne pollutant dispersion. Sensors are installed at 7 m height above ground. The sensor uses non-contact optical (Infrared) encoder technology for wind speed and non-contact hall-effect encoding for wind direction. Wind speed measurement range is upto 65 m/s with a resolution of 0.1 m/s. Wind direction measurement range is 0 to 358 degrees with a resolution of 1 degree.

(b) **Air Temperature and Humidity sensors** are designed for outdoor deployment in a weather shield (radiation shield). These two sensors measure air temperature and relative humidity as controlling parameters of atmospheric density and heat transfer process in air dispersion. Sensing Elements for Temperature is precision Resistance Temperature Detector (RTD) made of platinum thin film and for humidity it is dielectric capacitive sensor. Temperature measurement range is 0 to 55°C with a resolution of 0.1°C and a sampling interval of 10 s. Relative Humidity measurement range is 0 to 100% with a resolution of 1%. Sensors are installed at 2 m height above the ground.

(c) **Net Radiometer** measures Earth's net electromagnetic radiation (EMR), through the energy balance between incoming short-wave and long-wave IR radiation relative to surface reflected short-wave and outgoing long-wave IR radiation. Such measurement quantifies atmospheric thermal stability condition. This net radiometer includes two black conical absorbers; one facing upward, the other facing downward. Measurement range is (+/-) 2000 Watt/m². Response time of the sensor is 20s. It is installed at 2 m height above the ground.

(d) **Atmospheric Pressure Sensor** is a pressure transducer of range 600 to 1100 hPa to measure absolute pressure variations. The pressure transducer is provided with built-in electronics for signal conditioning with a response time of 1s. Sensor's spatial resolution is 0.1 hPa with a response time of 10 s. Sensor is installed at 1.5 m height above the ground.

(e) **Rain Gauge** measures rainfall, which is a direct fallout of air mass from the atmospheric system, hence reflects changes in the energetic of atmosphere. Rain Gauge uses the time tested tipping bucket mechanism along with the inclusion of modern electronics. It triggers a magnetic reed switch once for every unit of rainfall. Each pulse by Tipping bucket is counted by Digital Data Logger with in-built non-volatile memory. Rainfall measurement range is 0 to 1023 mm with a resolution of 0.5 mm. Sensor is installed at 0.25 m above the ground.

(f) **Environmental Radiation Monitor** is for measurement of natural background gamma radiation as well as elevated radiation levels in the environment. The system operates at ambient air temperatures between -20°C and +60°C and ambient relative humidity up to 100%. Two high sensitivity GM (Geiger Mueller) counters and 1 low sensitivity GM counter as radiation detectors are used for redundancy and to cover wide range of measurement (Fig. 2). The GM tubes are energy compensated with response range between 35 keV to 2 MeV. It can measure Gamma radiation in the

range 50 nGy/h to 20 Gy/h. Sensor is installed at 1.5 m height above the ground.



Fig. 2 ERM in waterproof multi-purpose box of ERM-AWS system along with Data Logger and UHF Transmission facility

Data logger and Transmission of Data

Data from all the sensors is integrated into a Data Logger. Usual time interval of data storing and transmission is 1 hour. In the case of gamma radiation level exceeding a pre-set threshold value, the data is transmitted every 5 minutes, till the value comes back to the background levels. The antenna is made of rust-resistant solid material having high gain with transmission at less than 10 Watts output. The data logger generates encrypted data and transmits through satellite telemetry using UHF Transmitter. To reduce the power consumption, only one way transmission i.e. from system to central station is activated, though the system is capable of two way communication.

Power Supply

The ERM-AWS operates on a single 12 Volts / 42Ah rechargeable SMF (Sealed Maintenance Free) battery,

which is charged with 40 Watt solar panel. This panel consists of series of connected mono crystalline silicon solar cells. The glass panel is self-cleaning in most climates, retains its excellent transmissivity indefinitely, and is extremely resistant to mechanical stresses.

Earth Station for Storing and Retrieval of Data

A dedicated stand-alone Earth Station has been established at Anushaktinagar, Mumbai, to receive online the data, decode and store encrypted data of respective ERM-AWS holding unique station ID. The earth station is assisted by an antenna array, which provides the communication link between the telecommunicating satellite and data receiving facility (Fig. 3). An antenna of 3.8 meters, indigenously designed by ISRO has been installed at the earth station. The antenna is used in the Rx (Receiver) mode only.



Fig. 3 Data receiving Earth Station at Anushaktinagar (a) 3.8 meter Receiver with Antenna (b) data Server

Receiving of data undergoes three tier system, i.e., data injection, data decoding and data view. Data view facility works through relational database management system whose primary function is to store and retrieve data as requested by users. The view facility is query based data display software. This shows list of installed ERM-AWS units, query based data retrieval for a specified normal as well as emergency period.

Application of ERM-AWS

In normal mode of operation, the system transmits hourly data. This will be useful to generate the baseline radiation data and climatology of the area. In case of an accident leading to increased gamma radiation levels, data is transmitted in 5 minutes interval as shown in Fig. 4. The system will be of use to generate early warning of increased radiation level along with site specific meteorological information. The simultaneous online meteorological data and radiation data can be used to derive the likely emission source release rate using inverse calculation in case of Nuclear Power Plants, and to drive the dispersion models to forecast radiological consequences and estimation of optimum countermeasures using real time online decision support systems like IRODOS (Indian Realtime Online Decision Support System) to handle offsite emergency, if any (Vinod Kumar et al., 2008).

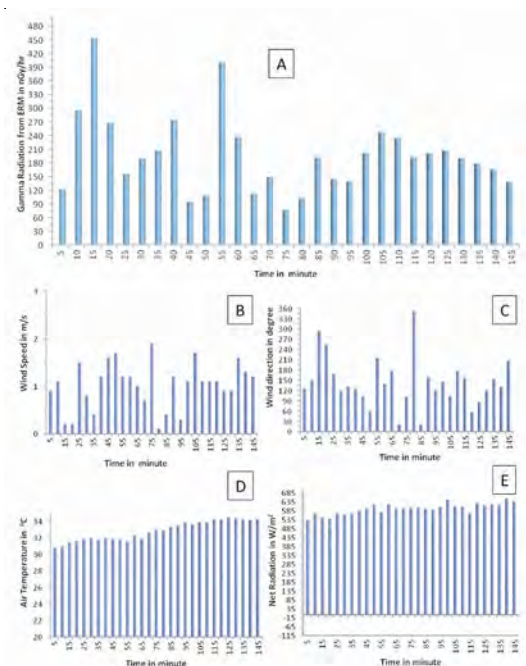


Fig. 4: A typical ERM-AWS data at an interval of 5 minutes in emergency mode (A=Atmospheric gamma radiation) (B= wind speed) (C=wind direction) (D= air temperature) (E=Net radiation due to solar insolation)

Conclusion

The state-of-the-art indigenous development of integrated ERM-AWS with seven meteorological parameters and one radiation level measurement is a technological advancement and is a useful system. Being indigenous and cost effective, it has a potential of being installed on a large scale at national level.

Acknowledgements

ERM-AWS system has been designed and developed under a MoU between BARC and ISRO. The AWS is a proprietary item of ISRO and ERM is a proprietary item of BARC. The integrated system has been produced by ANTRIX (Industrial Partner of ISRO), Bangalore through Astra Microwave Products Ltd., Hyderabad.

References

1. Manikiam B. and Murthy T.G.K. Technology development for atmospheric research and applications, Atmospheric Science Program Office, ISRO, Bangalore, 2008.
2. Vinod Kumar A., Oza R. B., Nair C. K. G., Awasthi A., Ratheesh M. P., Chaudhury P., Suri M. M. K., Saindane S., Singh K.D., Bhargava P., Anand S. and Sharma V. K. Online decision support system (IRODOS): an emergency preparedness tool for handling offsite nuclear emergency, *BARC News Letter*, 292, 2-6, 2008.
3. Patel M.D., Ratheesh M.P., Prakasha M.S., Salunkhe S.S., Nair C.K.G., Vinod Kumar A. and Puranik V.D. Multi-Detector Environmental Radiation Monitor with Multichannel Data Communication for Indian Environmental Radiation Monitoring Network (IERMON), *BARC News Letter*, 320, 31-34, 2011.
4. Garg S., Ratheesh M.P., Mukundan T., Patel M.D., Vinod Kumar A., Puranik V.D. and Nair C.K.G. The Architecture and Functions of Central Monitoring Station of Indian Environmental Radiation Monitoring Network (IERMON), *News Letter, Founder’s Day - Special Issue*, October, 419-422, 2011.

Radiography of 140 mm Thick Weld- Multiple Film Technique

S.P. Srivastava, S.P. Pandarkar, K.B. Santhosh, G.P. Sahu and S.B. Jawale
Centre for Design and Manufacture

Abstract

Radiography of 140 mm thick weld joints of Low Alloy Carbon Steel Cruciform Test Specimen was a challenging task due to radiation hazard attributed to large exposure time, high energy and high strength radiation source. High thickness of steel also adds to internal scatter within the specimen, reducing the quality of radiographs. Multiple film technique, which uses more than one film of same or different speed in a single cassette, was developed for panoramic exposure of four weld joints using cobalt 60 source. The technique was able to improve the quality of the radiographs besides reducing the exposure time by one third. This paper presents the detail of multiple film technique and its role in reducing the effect of thickness variation on the image quality.

Introduction

Under the Component Integrity Test Programme, Low Alloy Carbon Steel Cruciform Test Specimen are manufactured at Centre for Design and Manufacture (CDM) for biaxial load testing as a part of studies pertaining to safety aspects of Indian Pressurised Heavy Water Reactor. Specimens are made out of ASTM 508 Low Alloy Carbon Steel (20 MoNi55) in the shape of cruciform having unequal arms each of length 3300 mm and 1900 mm. Four slabs, each 135 mm thick x 300 mm wide, are welded to a symmetrical cross having two equal arms of length 175 mm (Fig. 1). Manufacturing process includes: Cutting of centre block and arms, Machining of centre block and arms for edge preparation, Machining of notches and slots in the centre block, Welding of arms with the centre block, Radiographic testing of weld joints and Post weld heat treatment.

As per the standard practice, symmetrical double V groove was adopted for butt weld joints between arm and centre block, considering very high thickness of 135 mm of the base metal. Further, in order to limit the distortion, heat input was minimized by reducing the volume of weld deposition. This was

achieved by machining the weld edge to compound bevel angles, thus making the groove narrower than the conventional groove. Ultrasonic testing (UT) was not feasible because of number of notches adjacent to the weld joint. Since radiographic testing (RT) was the only suitable NDE method for the volumetric examination of the weld, it was employed to detect lack of fusion (LOF) in the side wall, lack of penetration (LOP) at the root, porosity, crack and any other discontinuities existing in the weld. RT of thick specimen has inherent problems such as requirement of high strength source, very high internal scatter, high radiation hazard due to longer exposure time, low sensitivity for the portion away from the film. Any attempt to align the source with weld edge in order to detect lack of side wall fusion gives rise to large thickness variation demanding different exposure time for different shots. At CDM, multiple film technique for panoramic exposure was developed to radiograph all the four weld joints simultaneously. On account of reduced exposure time and less number of shots, this technique offers advantages of less radiation hazard, reduced scatter, high sensitivity and high productivity.

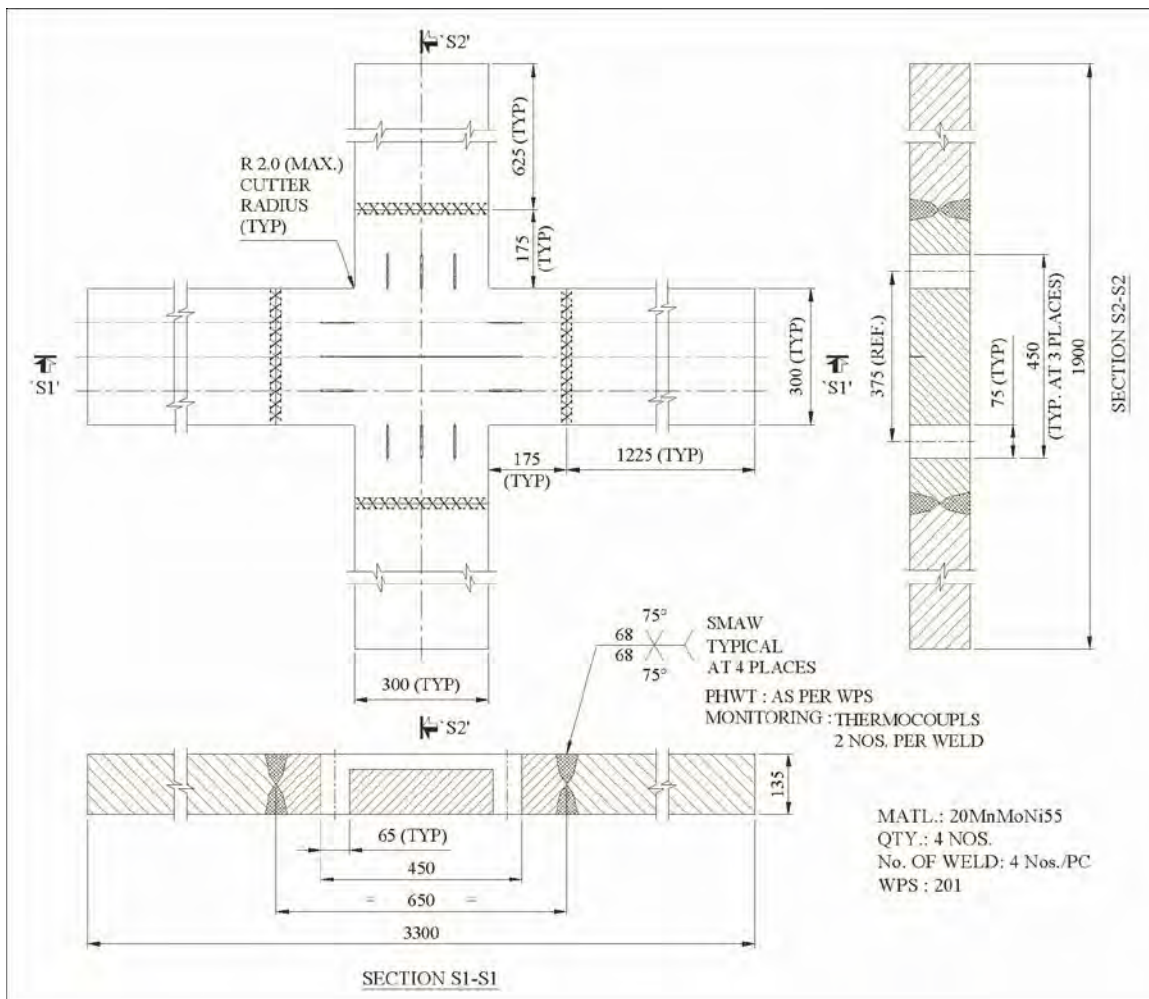


Fig. 1: Cruciform Test Specimen

Selection of NDT Method

Welds, with thickness less than 50 mm are examined by RT due to ease of interpretation and availability of image record. However, in case of RT of thick weld, radiation hazards are more due to high exposure time and high strength of radiation source required for radiography. Therefore, UT with no radiation hazard is considered a better choice for thickness 50 mm and above. Further, UT as compared to RT, gives better sensitivity for planar defects such as lack of fusion and crack. In order to detect lack of side wall fusion, welds are subjected to ultrasonic testing using angle beam technique. Particularly for thick weld, obstacle free large scanning area on both sides of the weld shall be available so that sound beam hits the side wall at

zero degree angle of incidence for better detectability of LOF. In this case, due to presence of slots in the scanning area UT was difficult, hence RT was considered suitable NDT method for volumetric examination of the weld.

Theoretical Considerations for RT of Thick Weld

In RT, direction of radiation beam with respect to the orientation of the flaw plays an important role for the flaw detectability. If the central beam is aligned with the major dimension of the flaw, the probability of flaw detection is very high. In groove weld, side wall and root are more vulnerable as far as defect is concerned. Radiographic shooting sketch (RSS) for butt weld with double V groove is shown in the Fig. 2. For single V groove weld having

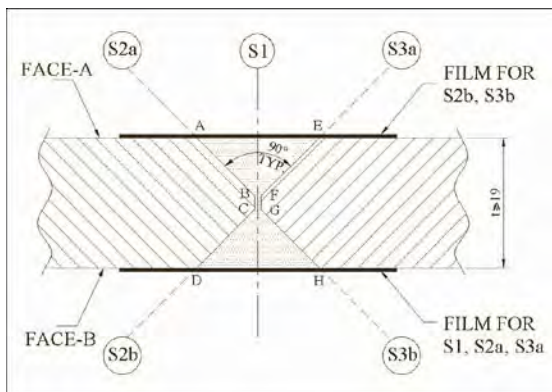


Fig. 2: RSS of double V butt weld in plate having thickness 80 mm or more

thickness less than 10 mm, even source at S1, aligned with root position can detect LOP in the root and LOF in the side wall as well. However, as the thickness increases, three different shots with source positions S1, S2a and S3a are required in order to detect LOP at root and LOF at each face. Object away from the film produces large geometrical unsharpness and therefore image of the weld groove which is away from the film will not be discernable, if thickness of the weld is more than 80 mm. Hence, beyond 80 mm thickness it is required to take shot from both sides of the weld, if accessible, to limit the unsharpness. Source positions S2a, S3a, S2b, and S3b are suitable for detecting LOF in walls GH, CD, EF and AB respectively. In case of cruciform, since the weld metal thickness including reinforcement was 140 mm similar shooting scheme was adopted for full volumetric examination of the weld.

Multiple Film Technique- Theoretical Aspects

In multiple film technique of radiographic testing, two or more films kept in close contact, are exposed together either to cover the varying thicknesses of the component or to reduce the exposure time. Films in combination may be either of same speed or different speed depending upon the requirement. In case of component of varying thicknesses, to improve the latitude i.e. range of thicknesses covered on the radiograph within acceptable density range of 1.0 to 3.5, combination of fast and slow film is exposed together and each film is viewed separately.

Fast film records thicker portion whereas slow film gives the detail of thinner portion.

In the second case, in order to reduce the exposure time, normally applicable for very thick job, two films of the same speed are exposed together which reduces the exposure time by one half. Combination of these films, when viewed separately will not meet density range of 1.0 – 3.5 individually and therefore will not reveal any detail. Such exposed films are viewed together i.e. by super imposing one on another in front of the viewing illuminator. The combined density of two films shall meet the density range of 1.3-4.0. In the technique developed at CDM in total two pairs of film were used, as explained in the subsequent paragraph, to get the advantage of both improved latitude and reduced exposure time.

Radiographic Testing of Weld Joints of Cruciform

Weld groove for butt joint in 300x135 mm cross section consists of symmetrical double V with 2 mm root land. Each V groove, includes two bevel angles; first one 75° starting from root up to 20 mm height and second one 24° starting from 20 mm up to 47.5 mm height (Fig. 3). Qualified welding procedure specification (WPS) and qualified welders were used for welding. All weld edges were checked for presence of any lamination by liquid penetrant test (PT). Root was fused by GTAW, and remaining weld was deposited by SMAW process. Pre-heating, with inter pass weld temperature control was done to avoid the formation of martensite and to prevent hydrogen induced cracks. Post weld heat treatment

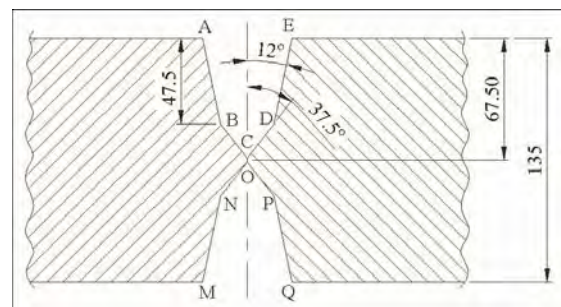


Fig. 3: Weld groove configuration

was adopted basically for stress relieving. Root pass welding and inter stage welding were subjected to RT and PT to detect any gross defect whose elimination after final pass requires lot of material removal by grinding process.

In order to detect lack of fusion in the side wall each weld joint in each arm requires at least five shots- one straight and four inclined shoots, two from each face. Though thickness penetrated in straight shot is 140 mm, interpretation is carried out only for half the thickness i.e. 70 mm of the weld which is closure to the film. Straight shot (SS) in which source and film are kept at SS1 and F1 respectively (Fig. 4), the total volume covered, is ABCDEx300 mm³ (Fig. 3). In this shot, because of its diverging nature, penetrating radiation is more or less parallel to faces AB and CD which are inclined at 12° with the vertical. Therefore, these shots are suitable for detecting any LOF in faces AB & CD and LOP at the root CO. Similarly by keeping source at SS2 volume MNOPQ can be examined with high degree of confidence for detecting LOP in faces MN and PQ.

Since faces BC (or CD) and NO (or OP) are inclined at 37° with the vertical and job thickness is more than 80 mm, to increase the probability for detecting LOF, it is necessary to take another radiograph with source in offset position, such that radiation beam is parallel to these walls. This requires two inclined

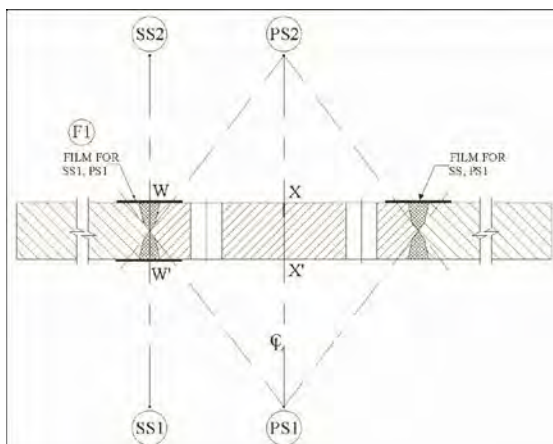


Fig. 4: RSS for panoramic shot for all four arms

shots with source at an angle with respect to weld axis WW'. Considering the symmetry of all the welds in each arm with respect to central axis XX', it was decided to use panoramic shot (PS) to radiograph all the four weld joints simultaneously in one shot, in order to reduce the total exposure time. In this set up, source is required to be positioned either at PS1 or PS2 on the central axis XX' of the cruciform such that the source to film distance (SFD) remains same for all the four weld joints with beam parallel to the walls inclined at 37° with the vertical.

Use of Multiple Film Technique for RT of Cruciform

Straight Shot: For straight shot with source at SS1 and film at F1 (Fig. 4), multiple film technique was used in which two films of same speed loaded in the same cassette were exposed to half the exposure time required for single film. Such exposed films were viewed together i.e. by super imposing one on another in front of the viewing illuminator. Since penetrometer was kept on full thickness, minimum SFD obtained by Equation 1 (Table 1) for $T = 140$ mm, $u_g = 1.7$ mm and $\phi = 7.5$ mm was 950 mm. During radiography, actual SFD was increased to 1100mm to minimize the divergence of the beam with respect to the face AB or DE. Exposure time for D7 single film using 40 curie cobalt source was estimated to 6 hour.

Inclined and Panoramic Exposure: Thickness across the weld cross section, seen by the radiation beam is different, because of the inclination and therefore it becomes essential to use multiple film to accommodate variation of optical density within acceptable limit. Radiographic setup for the panoramic exposure is shown in the Fig. 5. With its entire arm in horizontal plane, cruciform was kept above the source to take advantage of the shielding during panoramic exposure.

Ray diagram, using AutoCAD was prepared to know the source position, source to film distance and thickness variation for a set up which will give

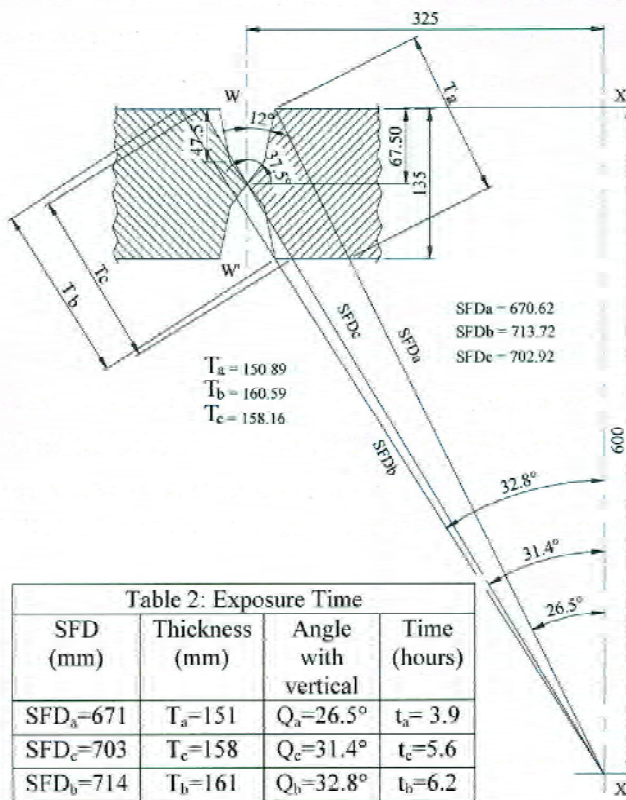


Fig. 5: Set up for panoramic exposure

adequate coverage of the weld with central beam parallel to face BC. Values of geometrical unsharpness were calculated using Equation 1 for three SFDs and thicknesses as shown in the Fig. 6. From the results of several iterations, with varying SFD and thickness, it was observed that for source at 600 mm, gamma ray from a point source was

parallel to the face BC within 6° and geometrical unsharpness was within the limit.

For source at 600 mm below the top surface of the cruciform on vertical axis XX', thickness, angle, and SFD with exposure time for each combination, are tabulated in Table 2. Exposure time were calculated using Equation 2, which is basically applicable to narrow beam geometry and is meant only as a guide for knowing approximate exposure time. Actual exposure time is established by trials rather than formula as it depends on the accuracies of many variables such as source size and its strength, SFD, film processing time/condition, scatter radiation etc. For very thick specimen actual exposure time is less than the calculated one, due to internal scatter contributed by the specimen itself. During trial shot, using fast film Agfa D7, it was observed that even with low exposure time, film density for the thickness



SFD (mm)	Thickness (mm)	Angle with vertical	Time (hours)
$SFD_a = 671$	$T_a = 151$	$Q_a = 26.5^\circ$	$t_a = 3.9$
$SFD_c = 703$	$T_c = 158$	$Q_c = 31.4^\circ$	$t_c = 5.6$
$SFD_b = 714$	$T_b = 161$	$Q_b = 32.8^\circ$	$t_b = 6.2$

Table 1: Formula

Calculation of SFD, based on u_g
 $SFD = T \left(1 + \frac{\phi}{u_g} \right)$ ---(Equation 1)
 SFD = Source to film distance.
 T = Thickness penetrated.
 u_g = geometrical unsharpness
 ≤ 1.7 mm, for $T \leq 100$ mm
 ϕ = Effective source size
 $= \sqrt{d^2 + l^2}$
 d and l are diameter and length of a cylindrical source.
 Calculation of Exposure Time:
 $t = \frac{FF.SFD^2.2^{n.60}}{Ci.RHM.100^2}$ ---(Equation 2)
 t = Exposure time in minute,
 FF = Film factor,
 SFD = Source to film distance in cm,
 $n = \frac{\text{Thickness penetrated}}{\text{Half value thickness}}$
 Ci = Source strength in curie,
 RHM = Roentgen hour meter

Fig. 6: Ray diagram for panoramic exposure using multiple film

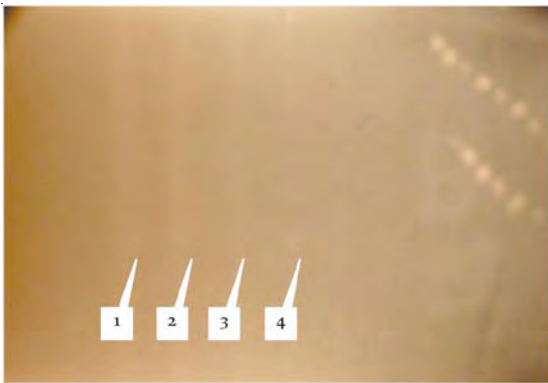


Fig. 7: Single film with 1.63 optical density

T_a and SFD_a , was on higher side and therefore to offset this, slow film Agfa D4 was considered a better option as compared to Agfa D7 film.

To reduce the exposure time, combination of fast (D7) and slow (D4) films was found suitable for lower thickness region ' T_a ' whereas combination of two fast films (D7) were adequate for higher thickness regions ' T_b ' and ' T_c '. To take care of the continuous variation in the thickness and for the continuity of the weld image, one large size D7 film, overlapping the total thickness range was used. All the three films with their relative positions, were loaded in a single cassette. Film were exposed for 3 hours 30 minutes, which is approximately one half the maximum exposure time $T_b = 6$ hours 12 minutes and greater than the half of the minimum exposure time i.e. 3.9/2 hours.

Tungsten arrow markers were placed on the film as well source side to show the coverage of the weld width and projection of the source side weld image on the film. In total three image quality indicators (IQI), two for source side and one for film side were placed to check the adequacy of the image quality.

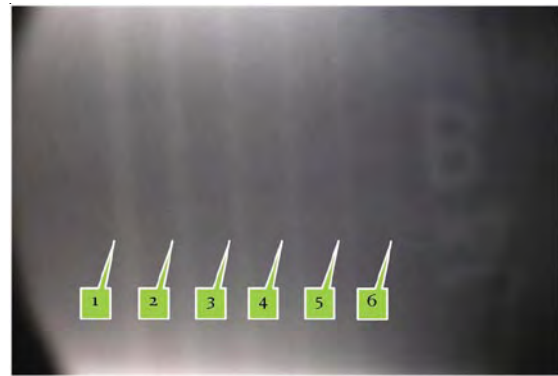


Fig. 8: Double film with 3.32 optical density

Interpretation of Multiple Films

During interpretation of radiographs, two D7 films were viewed together for thicknesses ' T_b ' and ' T_c '. For thickness ' T_a ', because of adequate density only one film either D7 or D4 can be viewed individually, however, if D7 and D4 are viewed together, better perception of the IQI image is obtained. As per the ASME requirements, image of the 4T hole in 60 number plate type IQI was seen when both the films were viewed together. In addition to plate type IQI, wire type IQI No.1 ISO 7 (DIN) was also used, for which 5th wire image was seen. Weld at intermediate stage having thickness of 110mm was radiographed using two films of same speed at half the exposure time required for single film. Fig. 7 and Fig. 8 are radiographic images of single film and superimposed double film respectively. On single film, with optical density 1.63, even image of the fourth wire of a wire type penetrameter is not seen clearly, whereas two films superimposed and viewed together is able to reveal well defined image of the fifth wire and slightly faint indication of the sixth wire. Besides wire, images of letter B and J4 are clearly seen in Fig. 8.

Table 3: Comparison between single and multiple film technique

S. No.	Exposure Type	Source Position	Shots per arm	Time per shot (hour)	Shots for four arms	Total Time (hour)	
						Single Film	Multiple Film
1.	Directional	SS1 & SS2	2	6	8	48	24
2.	Directional	PS1 & PS2	2	6.2	8	49.6	24.5
3.	Panoramicl	PS1 & PS2	2	6.2	2	12.4	6.2

Conclusions

Radiography of thick weld requires proper planning to take care of flaw detectability, scatter radiation, high exposure time, large value of unsharpness, shielding to reduce the radiation hazard, IQI sensitivity etc. At CDM, multiple film technique was developed to address these problems. Review of exposure time (Table 3) indicates that total exposure time for four welds of a cruciform is 97 hour when single film is used with directional exposure. Whereas time for panoramic exposure combined with multiple film technique is only 30.2 hour, which is approximately one third (31%) of the total time.

Multiple film technique with panoramic exposure not only reduced the exposure time but also minimized the density variation along the composite film from one end to another end.

References

1. Richard A. Quinn and Claire C. Sigl, *Radiography in Modern Industry, Fourth edition*. EASTMAN KODAK COMPANY, Rochester, New York 14650
2. Nondestructive Inspection Methods Manual, Section VI, Special Radiographic Techniques, TM-1-1-1500-335-23, Integrated Publishing, <http://www.tpub.com>

Critical Design Review of the MACE Gamma-Ray Telescope: Status Report

The 21m diameter MACE (Major Atmospheric Cherenkov Experiment) gamma-ray telescope is being set up by BARC in collaboration with TIFR and IIA, to explore the high energy Universe in the hitherto unexplored energy region of 20-100 GeV and beyond. The telescope is manufactured by ECIL and is being installed at Hanle (32.8°N, 78.9°E, 4200m asl), a high altitude astronomical site in the Ladakh region of North India. It consists of a large area tessellated light collector (356m²) made up of 356 mirror panels each comprising of 4 pre-aligned metallic mirror facets of 488mm x 488mm size with a graded radius of curvature of 50 – 52m. A 1088 pixel imaging camera with a resolution of 0.125° is deployed at the focal plane of the telescope to detect and characterize the feeble short duration (~ 5ns)

Cherenkov flashes produced in the atmosphere by the incident gamma-ray photons and charged particles. The large f-number of 1.2 coupled with the camera weight of 1200kgs and the pointing/tracking accuracy requirement of better than 1 arc-min introduces stringent constraints on the mechanical design of the structure. The telescope also has a quick pointing mode where in it can point to any direction in the sky within 75 sec. In view of the difficult site conditions at Hanle it was decided to erect a proof-assembly of the telescope at ECIL, Hyderabad and validate its various sub-systems. The proof assembly of the telescope has been recently completed and followed by a Critical Design Review.



The picture on the left shows 8 mirror panels installed around the centre of the mirror basket. The servo TDU and TCU are installed in the instrumentation shelter mounted on the adelaide structure. The picture on the right shows the participants of the CDR meeting gathered in front of the proof-assembly

The Critical Design Review Committee was set up by Director, BARC under the chairmanship of Prof. S. Anathakrishnan, former Observatory Director, GMRT, Pune. The other members of the committee are Prof. P.Sreekumar, Director, IIA, Bangalore, Shri G.P.Srivastava, former Director, E&I Group, BARC, Shri S.C.Tapde, former Project Director, GMRT, Pune. The committee met on 11th and 12th June 2014 at ECIL, Hyderabad. The design teams from BARC and ECIL presented the status of various sub-systems of the telescope along with the test results. The prototype version of imaging camera electronics consisting of 16 channel Camera Integrated Modules and back-end electronics i.e. Central Camera Controller, Data Concentrator and Second Level Trigger generator was integrated and tested in the actual telescope environment. The Operator Console was installed at the Ground Station and the full functionality with respect to configuration, monitoring and event acquisition of Imaging Camera, interface to Telescope Control Unit, Observation Scheduler and Run Manager was tested and demonstrated during the Critical Design Review. The committee also witnessed a demonstration of the dual axis drive system and the mirror alignment system of the telescope.

It was brought out that the mechanical structure of the 180 tonne telescope has been assembled to the required accuracy levels. The lessons learnt during the proof assembly will be helpful during the final assembly at Hanle. Eight mirror panels of 984mm x

984mm have been mounted on the telescope and their alignment checked with a light source mounted at a distance of ~250m. The servo control drive system of the telescope has been fully validated and fine tuned to obtain required responses and tracking accuracy of better than 10 milli degrees (<0.5 arc-min). The natural frequency in azimuth and elevation has also been determined experimentally by the locked rotor test. These frequencies are 1.7 Hz in azimuth and 1.4 Hz in elevation.

Based on the test reports and the performance of the proof-assembly CDR committee recommended the dismantling and transportation of the telescope to Hanle. Part of the structure will be assembled at Hanle during Sept-Oct 2014 while the rest will be completed during May-Oct.2015. The telescope is likely to see first light with Crab Nebula observations in Dec. 2015 and be fully operational by the summer of 2016.

The design, manufacturing and assembly of this indigenously developed, one of a kind, instrument is the result of collaborative efforts of many Indian scientific organisations and industry partners. Many Divisions of BARC have contributed to the development of various subsystems of the telescope viz., Astrophysical Sciences Division, Atomic and Molecular Physics Division, Centre for Design and Manufacture, Computer Division, Electronics Division, Precision Engineering Division, Reactor Control Division and Reactor Safety Division.

Report on Eleventh ISEAC International Discussion Meet on Electrochemistry and its Applications (11th ISEAC-DM-2014)

The Eleventh ISEAC International Discussion Meet on Electrochemistry and its Applications (11th ISEAC-DM-2014) was held at Amritsar, India during February 20-25, 2014. The Discussion Meet was organized under the aegis of the Indian Society for ElectroAnalytical Chemistry (ISEAC) having its secretariat at Fuel Chemistry Division, Bhabha Atomic Research Centre, Mumbai, India.

The Discussion Meet was attended by about 150 participants with 20 foreign nationals from 12 countries and delegates from different parts of India. The inauguration function was held in the evening of February 20, 2014 at the venue. Prof. S.K. Aggarwal, President, ISEAC and Chairman, Organising Committee welcomed all the delegates of 11th ISEAC-DM-2014 and briefed the about the activities of ISEAC since its inception in October, 2003. Mr. Saurav K. Guin, Secretary, ISEAC and Convener, Organising Committee presented a summary about the various topics both fundamental

and applied Electrochemistry, to be discussed during the meet. Prof. (Mrs.) Ana Maria Oliveira Brett from Portugal, President of Bio-Electrochemical Society (BES) formally released the bound Volume of the Conference Proceedings (Edited by Suresh K. Aggarwal, Saurav K. Guin, Ruma Gupta and Arvind S. Ambolikar; 276 pages; ISBN 978-81-901950-6-5). Prof. S.K. Aggarwal formally released the Souvenir-cum-Bulletin of ISEAC entitled Highlights in ElectroAnalytical Techniques (HEAT), Volume 3, Issue I, 2014. Mr. Saurav K. Guin formally released the CD-ROM of the Proceedings and HEAT. Mr. Arvind S. Ambolikar, Secretary, Organising Committee proposed a vote of thanks.

11th ISEAC-DM-2014 was spread over 16 technical sessions covering 32 invited talks, 6 short invited lectures, 67 poster presentations, 12 oral presentations by research scholars and 1 vendor's presentation. Invited speakers from overseas included Prof. H. Terryn (Belgium); Prof. K. Vytras and Prof.



Participants of Eleventh ISEAC International Discussion Meet on Electrochemistry and its Applications (11th ISEAC-DM-2014)

R. Metelka (Czech Republic); Dr. Frederic Maillard, Dr. J. Gaubicher and Dr. Valentina Ivanova (France); Prof. D. Fattakhova-Rohlfing (Germany); Prof. Hiroshi Nishihara (Japan); Dr. Keith Baronian (New Zealand); Prof. W. Kutner (Poland); Prof. Christopher M.A. Brett and Prof. (Ms.) A.M. Oliveira-Brett (Portugal); Prof. Sangaraju Shanmugam (Republic of Korea); Dr. Chee-SengToh, Prof. Harry Ernst Hoster and Dr. M.V. Reddy (Singapore); Prof. Lo Gorton (Sweden); Dr. Carsten Schwandt, Prof P. Vadgama and Prof. Ritu Katakya (UK). The speakers from India included Prof. Rakesh Kumar Mahajan (Amritsar); Prof. Rama Kant and Prof. Suddhasatwa Basu (Delhi); Prof. S. Balaji (Kanchipuram); Dr. R. Mukhopadhyay (Kolkata); Prof. A.Q. Contractor and Dr. S.K. Ghosh (Mumbai); Prof. R.N. Patel (Rewa); Prof. A.C. Hegde (Surathkal) and Prof. Annamalai Senthil Kumar (Vellore). The short invited lectures were delivered by Dr. Sudhanshu Sharma (Ahmedabad); Dr. Murali Rangarajan (Coimbatore); Dr. Rahul Pal (Delhi); Dr. Alka Sharma; Dr. A.K. Satpati and Mr. Saurav K. Guin (Mumbai, India).

Interactive discussions took place during the technical sessions on the applications of electrochemical atomic force microscope and other *in-situ* characterization techniques during electrochemical experiments. Other areas of discussion were advanced batteries, fuel cells, electrochemical capacitors, analytical environmental electrochemistry, bioelectrochemistry, biosensors, biofuel cells, corrosion science and engineering, role of electrochemistry in health, medical and nuclear science, electrodeposition, electrochemical engineering, impedance spectroscopy, electrochemistry in ionic liquids and molten salts, physical, theoretical and computational

electrochemistry etc. A Panel Discussion on "Emerging Trends in Electrochemistry" was also conducted during the Discussion Meet. A special session viz. "Unconference" was organized to discuss the technical aspects, suitability of the instruments, personal working experience, discussing about companies selling instruments etc. About 16 abstracts were shortlisted to be reviewed for publication in the Special Issue viz. "Electroanalysis in India" in Electroanalysis Peer-Reviewed Journal, with Dr. S.K. Aggarwal as Guest Editor.

During the valedictory function, some of the delegates gave their impressions about the event and expressed satisfaction over the high quality of technical discussions and overall arrangements. Prof. Brett represented the International Society of Electrochemistry (ISE) and highlighted the activities of ISE. Merit certificates and cash awards were given to the authors of three best posters and one best oral presentation evaluated by a Committee chaired by Prof. Kutner. Prof. Aggarwal thanked all the delegates, as well as sponsors and advertisers, for their support during the deliberations of the Conference. In particular, he thanked the International Society of Electrochemistry (ISE) and Bioelectrochemical Society (BES) for their financial support. He also thanked the members of the Advisory Committee and members of the Organizing Committee. Mr. Saurav K. Guin, Convener of the Discussion Meet proposed a vote of thanks. Dr. Aggarwal informed all the delegates about the 12th ISEAC-2015 to be held at Cochin during January 12-16, 2015. He requested them to visit ISEAC website (www.iseac.org) and also invited suggestions for the Event.

IAEA Regional Training Course on “Security in the Transport of Radioactive material”

The Secretariat of BARC Safety Council, BARC and International Atomic Energy Agency (IAEA) jointly organized a IAEA Regional Training Course(RTC) on “Security in the transport of radioactive material” during 3-7 March 2014 at Navi Mumbai.

The purpose of the regional training course was to increase awareness regarding need for increasing security during the Transport of Radioactive Material. The course provided the participants with the necessary knowledge to develop and implement national transport security requirements. Representatives of law enforcement agencies, regulatory bodies and operators were benefited from learning about specific security measures and technologies that may be used as part of national nuclear security system. The course was based on the guidance provided in Nuclear Security Recommendations on Radioactive Material and

Associated Facilities (IAEA Nuclear Security Series No. 14), as well as in Security in the Transport of Radioactive Material (IAEA Nuclear Security Series No. 9).

Twenty four participants from various countries including India, UAE, Malaysia, Jordan, Lao, Indonesia, Yeman, Lebenon and Behrain participated in the RTC. They represented regulatory body, utility and transport organizations. Indian delegates comprised of the regulators from AERB and BSC, BRIT, NRB, NRG, PDD, Crisis Management Group, DAE and Security Section, BARC. Mr. Jose Joseph, Head, BSCS and Course Director of this course and Mr. Stig Isaksson, IAEA Scientific Secretary welcomed the delegates on the opening day of the meeting. Mr G. Gouthaman, Chairman, BSC threw light on the theme of the course and Dr. D.N. Sharma, Director, HS&EG inaugurated the course. The course



Inaugural function of IAEA-RTC: From left to right: Mr. Jose Joseph, Head, BSCS, Shri G. Gouthaman, Chairman, BSC; Dr. D.N. Sharma, Director, HS&EG; Mr. Stig Isaksson, IAEA Scientific Secretary



Mr. Jose Joseph, Head, BSCS and Course Director delivering the lecture

was designed with 12 modules and exercises. The instructors from IAEA were Mr. Dragan Krkljuš, Serbia, David Allen Duhamel, USA and Dr. A.N. Nandakumar, Ex. AERB, India.

Mr. Jose Joseph, Head, BSCS and Course Director delivered the lecture on "The need for Transport Security". Mr. S.K. Garai, BSCS and Mr. A.S. Vajarekar, BSCS delivered lectures on the modules Enhanced and additional security Measures. Mr. R.K. Singh, RSD, AERB delivered lecture on Transport Security in India Specific Regulations and

Requirements / Responsibilities of consignors, carriers, consignees. Talks from various delegates on their country specific experience with the activities related to regulations on transport security and responsibilities of Consignor, Carriers and Consignees and implementation. The exercise on development of transport security plan and workshop on security transport readiness review were conducted.

There was a feedback survey from all the participants and instructors during the course. The course was concluded by valedictory function with the grace of Mr. G. Gouthaman and Dr. A.K. Kohli, CE, BRIT. The IAEA officials, faculties and chief guests were felicitated. On successful completion of the training course all the participants were presented with certificates from IAEA. The course content in the printed modules, photograph in form of contact book and CD were distributed to participants. The course was conducted by Mr. S. Isaksson, IAEA; Mr. Jose Joseph, Head, BSCS and Mr. R.P. Hans, Head, SR&RSS, BSC Secretariat, and as contact point for the course under the valuable guidance of Mr. G. Gouthaman, Chairman, BSC.

National Conference (IARPNC-2014) : a Report

The Indian Association for Radiation Protection organised its 31st National Conference (IARPNC-2014) on the “Advances in Radiation Measurement Systems and Techniques” at Multipurpose Hall, BARC Training School Hostel, Anushaktinagar, Mumbai during March 19-21, 2014. The conference was attended by about 400 scientists, including Radiation Protection professionals from DAE, IAEA, DRDO, industry. Invited speakers both from India and abroad shared their expertise and important insights in the field of radiation protection. One of the important features of the conference was the participation of a large number of students and professors from various universities from all over India.

The scientific deliberations of the conference included latest systems and techniques developed for radiation measurements, environmental radioactivity, assessment of radiation exposure to the public from natural radiation and emergency preparedness. There were thirteen invited talks; notable amongst them were the ones on Fukushima accident by Dr. T. Suzuki, an IAEA expert from Japan, Epidemiological investigations by Dr.K.B. Sainis, Former Director, BMG and Dr. R.A.Badwe, Director, Tata Memorial Centre, Mumbai. Dr. Sainis noted that comprehensive data from high background radiation areas of Kerala from a cohort of more than 300,000 persons exposed to high levels of natural radiation did not show any incidence of excess cancer rates over the incidence

rates in normal population. These studies lead to non-applicability of linear no threshold (LNT) model at least for doses below 100 mSv. Dr. Badwe informed that the cancer incidence rates are about 40 for 100,000 persons in rural areas and about twice of this in the urban areas. The extensive studies undertaken by TMC, have also not indicated any additional cancer incidences, attributable to power plant operations in different regions in India as compared to those observed in nearest control population.

There was a lively panel discussion on ‘Nuclear Power, Radiation Protection and Public Perception’ on the concluding day of the conference. The panelists included experts from BARC, AERB, NPCIL and DAE. Many panelists expressed their views that based upon the international research, there could be a possibility of a threshold dose below which there is no risk for exposure to external radiation or more beneficial as predicted by radiation hormesis.



Release of the book of abstracts during the inaugural function of IARPNC-2014

Dignitaries (from L to R) : Dr. K.S.Pradeepkumar (Head, RSSD, BARC), Shri S.S. Bajaj (Chairman, AERB), Shri B.Bhattacharjee (Hon. Member, NDMA, New Delhi), Dr. D.N.Sharma (Director, HS&EG) and Dr. M.S.Kulkarni (Convener, IARPNC-2014)

National Conference on Rare Earth Processing and Utilization-2014 (REPUT-2014) : a report

The Two day national conference on “Rare Earth Processing and Utilization-2014” was jointly organized by Rare Earth Association of India, Indian Institute of Metals-Mumbai Chapter, Materials Research Society of India-Mumbai chapter and Board of Research in Nuclear Studies. The conference was held at Multipurpose Hall of Training School Hostel, Anushaktinagar, Mumbai, during May 2-3, 2014. The event provided a scientific communication platform for scientists, engineers, technologists and industry working in the areas of science, technology and applications of rare earths and contributed towards the scope of further development in new technologies and applications of rare earths in India.

The conference was inaugurated by Dr. Ratan Kumar Sinha, Chairman, AEC and Secretary, Department of Atomic Energy, Government of India. Dr. R. N. Patra, Chairman, National Organizing Committee & CMD, IREL gave overview about the theme of the symposium and highlighted the importance of rare earths industry in the country and role they play in various advanced technology areas. Four technical sessions consisting of 17 invited lectures covering the entire spectrum of rare earths prospecting, processing and utilization in India was arranged. There were 50 contributory papers which were presented in the

poster session. A panel discussion chaired by Dr. S. Banerjee, Homi Bhabha Chair Professor, HBNI with members from different parts of the country in the field, was held to discuss the roadmap for rare earth processing and utilization in the country.

In order to encourage young scientists working in the field of rare earths, two best poster awards were given. The first prize was given to Dr. S. P. Radhika, CLRI, Chennai, for the poster entitled “Introducing multifunctionality into rare earth pigments : Coupling benign and cool” and the second award was given to Dr. Pushpal Ghosh of Dr. H. S. Gour University, Madhya Pradesh for the poster entitled “Facile preparation of quantum cutting $\text{NaGdF}_4:\text{Eu}^{3+}$ nanoparticles from ionic liquids”.

The organizing committee sincerely thanks BARC management for providing necessary support required for successful completion of the national conference REPUT – 2014.



Inaugural talk by Dr. Ratan Kumar Sinha, Chairman, AEC and Secretary, Department of Atomic Energy, Government of India.

Conference on “75-years of Nuclear Fission: Present status and future perspectives”

Nuclear fission was discovered 75 years ago and is considered to be one of the most important scientific discoveries in basic and applied nuclear research. It has played a key role in the understanding of statistical and dynamical properties of nuclei, in the production of nuclear power, development of nuclear instrumentation and evolution of other related fields. In order to commemorate this occasion, a conference on “75 years of Nuclear Fission: Present status and future perspectives” was organized by Nuclear Physics Division, Bhabha Atomic Research Centre, Mumbai during May 8-10, 2014 at the Nabhikiya Urja Bhavan Auditorium, Anushaktinagar. The conference was sponsored by the Board of Research in Nuclear Sciences (BRNS). The main goal of the conference was to review the progress in the understanding of nuclear fission during past 75 years and also to indicate the direction of future research in fission. Nuclear fission occupies a prominent place in the context of global energy resources, and has

given impetus to scientists and engineers to look at advanced reactors for the production of cost effective nuclear power.

The conference provided a scientific forum for participants to discuss their work and interact with other researchers in the field of nuclear fission and related areas. It provided a wide exposure of nuclear fission studies using advanced reactors, accelerators and detector systems, spanning a wide range of topics of current interest. There was an enthusiastic response from the participants across the globe to discuss various aspects of nuclear fission. There were about 200 participants in the conference including 17 from abroad. The one-page abstracts from 45 invited speakers and 56 contributed papers for poster presentations were published in an abstract book. The research papers covered topics in the field of fission process, fission fragment spectroscopy, radiochemical studies in fission, cluster radioactive decay, superheavy element studies and various



From Left: Dr. S.S. Kapoor, Prof. V.S. Ramamurthy, Dr. R.K. Sinha, Dr. V.M. Datar, Dr. D.C. Biswas



A group photograph of the participants of Fission75 conference

applications of fission data. The role of nuclear fission in the design of advanced nuclear reactors, radioactive ion beam production and development of sophisticated experimental techniques were highlighted.

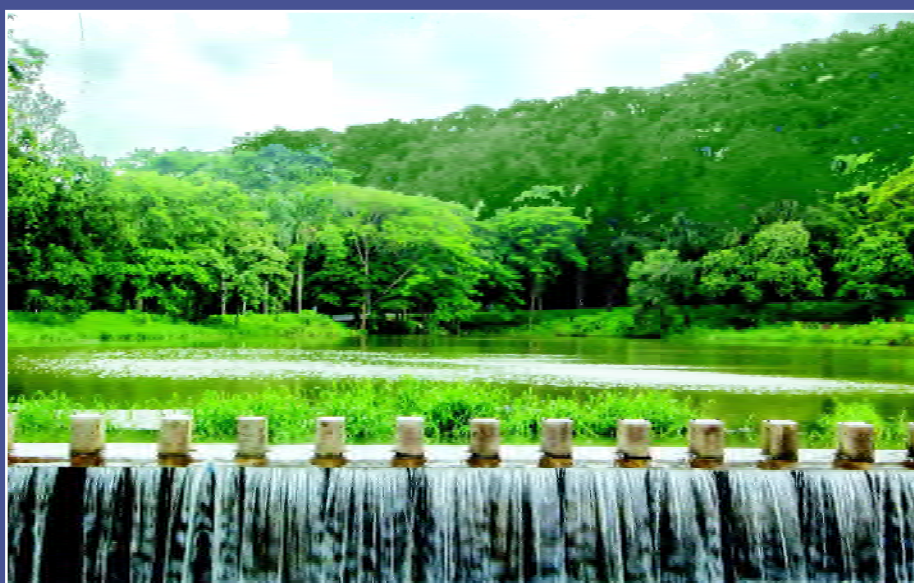
In his welcome address Dr. V.M. Datar, Chairman of the organizing committee, mentioned about the goals of the conference in the context of nuclear fission research programme in BARC. Prof. V.S. Ramamurthy, Director, National Institute of Advanced studies (NIAS) and former Secretary, DST, delivered the keynote address. He emphasized the relevance of basic research in the understanding of nuclear fission processes and its application in various fields. Dr. R.K. Sinha, Chairman, Atomic Energy Commission inaugurated the conference and highlighted the progress of nuclear science and engineering since the discovery of fission in 1939. He has made special mention of the role of fission for the production of nuclear energy in the service

of mankind. Dr. S.S. Kapoor, INSA Honorary scientist and former Director, Physics Group, BARC gave an overview of the nuclear fission research and mentioned that it is one of the landmark discoveries in Nuclear Physics. He presented some of the exciting results on superheavy elements and also discussed the possibility of accelerator driven sub-critical reactor system for nuclear power production. In the inauguration function, the formal vote of thanks was given by Dr. D.C. Biswas, Convener of the conference.

Many eminent scientists from BARC and Indian Universities, who have made significant contributions in the fields of nuclear fission for last many decades, participated in the conference. There was a special reminiscences session on May 09, 2014, to recollect their involvement in the growth and development of research activities on nuclear fission and related fields in India. Dr. S. Kailas, former Director, Physics Group, BARC delivered the summary talk of the conference.

BARC Scientists Honoured

- Name of the Scientist :** **Shri Mani Krishna Venkata Karri, Materials Science Division**
- Name of the Award :** INSA Medal for Young Scientists, 2014
- Instituted by :** Indian National Science Academy
Has been working on phase transformations and deformation of h.c.p materials. A unique feature of his work is the combination of experiment and computer simulations to address issues that are of both academic and industrial significance.
- Name of the Scientist :** **Shri Prakash Chandra Rout, Nuclear Physics Division**
- Name of the Award :** INSA Medal for Young Scientists, 2014
- Instituted by :** Indian National Science Academy
For his significant contribution in developing a large area scintillator detector for the measurement of fast neutrons using the time of flight technique and for his studies on the damping of nuclear shell effect in the doubly magic 208Pb region.
- Name of the Scientist :** **Dr. Ashish Kumar Srivastava, Nuclear Agriculture and Biotechnology Division**
- Name of the Award :** INSA Medal for Young Scientists, 2014
- Instituted by :** Indian National Science Academy
His work emphasizes that thio urea supplementation upregulates the expression of sulphate transporters that improve sulphur assimilation associated with redox signaling.



Pond at Trombay, BARC

Edited & Published by:
Scientific Information Resource Division,
Bhabha Atomic Research Centre, Trombay, Mumbai 400 085, India
BARC Newsletter is also available at URL:<http://www.barc.gov.in>